Time-ordered data simulation and map-making for the PIXIE Fourier transform spectrometer

S. K. Næss[1,2], J. Dunkley[2,3,4], A. Kogut[5], and D. J. Fixsen[5,6]

[1]Center for Computational Astrophysics, Flatiron Institute
[2]Oxford Astrophysics, Keble Road, Oxford, OX1 3RH, UK
[3]Princeton Physics, Jadwin Hall, Washington Road, Princeton NJ 08544
[4]Princeton Astrophysics, Peyton Hall, Ivy Lane, Princeton NJ 08544
[5]Goddard Space Flight Center
[6]University of Maryland

July 27, 2021

Abstract

We develop a time-ordered data simulator and map-maker for the proposed PIXIE Fourier transform spectrometer and use them to investigate the impact of polarization leakage, imperfect collimation, elliptical beams, sub-pixel effects, correlated noise and spectrometer mirror jitter on the PIXIE data analysis. We find that PIXIE is robust to all of these effects, with the exception of mirror jitter which could become the dominant source of noise in the experiment if the jitter is not kept significantly below $0.1\mu\mathrm{m}\sqrt{\mathrm{s}}$. Source code is available at `https://github.com/amaurea/pixie`.

1 Introduction

In 1989 the COBE experiment fielded two instruments that would revolutionize the study of the cosmic microwave background (CMB): the differential microwave radiometer (DMR), which provided the first measurement of the angular power spectrum (Smoot et al., 1992); and the far-infrared absolute spectrophotometer (FIRAS), which measured its frequency spectrum and showed it to be blackbody to exquisite precision (Fixsen et al., 1996). Since then DMR has been succeeded by a large number of experiments that have improved the angular power spectrum by several orders of magnitude both in sensitivity and angular resolution (Bennett et al., 2013; Planck Collaboration, 2013; BICEP2/Keck and Planck Collaboration, 2015; ACT Collaboration, 2017; Henning et al., 2017). However, the nearly 30 year old FIRAS result remains our best measurement of the CMB frequency spectrum.

The Primordial Inflation Explorer (PIXIE) is a proposed successor to FIRAS, with $\sim$ 1000 times higher sensitivity, polarization support, 4 times higher angular resolution and reduced systematics. It would provide 1.6° FWHM full-sky maps in Stokes I, Q and U parameters in 480 frequency channels from 15 GHz to 7 THz (though it would be noise dominated beyond ca. 4 THz) to a depth of 70nK° (that is, a square degree variance of 1400 nK^2) after 4 years of integration (Kogut et al., 2011). This corresponds to providing a frequency spectrum 10 times more sensitive than FIRAS CMB monopole spectrum in each 1° pixel of the sky. That is sufficient to constrain the spectral distortion parameters to $\mu < 4 \cdot 10^{-7}$ (probing the ultra-small-scale primordial power spectrum and exotic pre-recombination particle decay) (Abitbol et al., 2017) and $y < 2 \cdot 10^{-9}$; to measure the optical depth at reionization to $\sigma(\tau) = 0.002$ (essential for getting a robust neutrino mass measurement); and to measure the tensor-to-scalar ratio to $\sigma(r) < 0.001$ (Calabrese et al., 2017). And crucially, PIXIE's dense and broad frequency coverage would allow for robust foreground separation, especially dust.

To make use of these huge increases in sensitivity, a corresponding reduction in systematic errors is needed. PIXIE's systematics were studied in detail by Nagler et al. (2015), who concluded that any residual errors after corrections would be at the sub nK level, far below the instrumental noise. However, so far no end-to-end simulations of PIXIE have been performed.

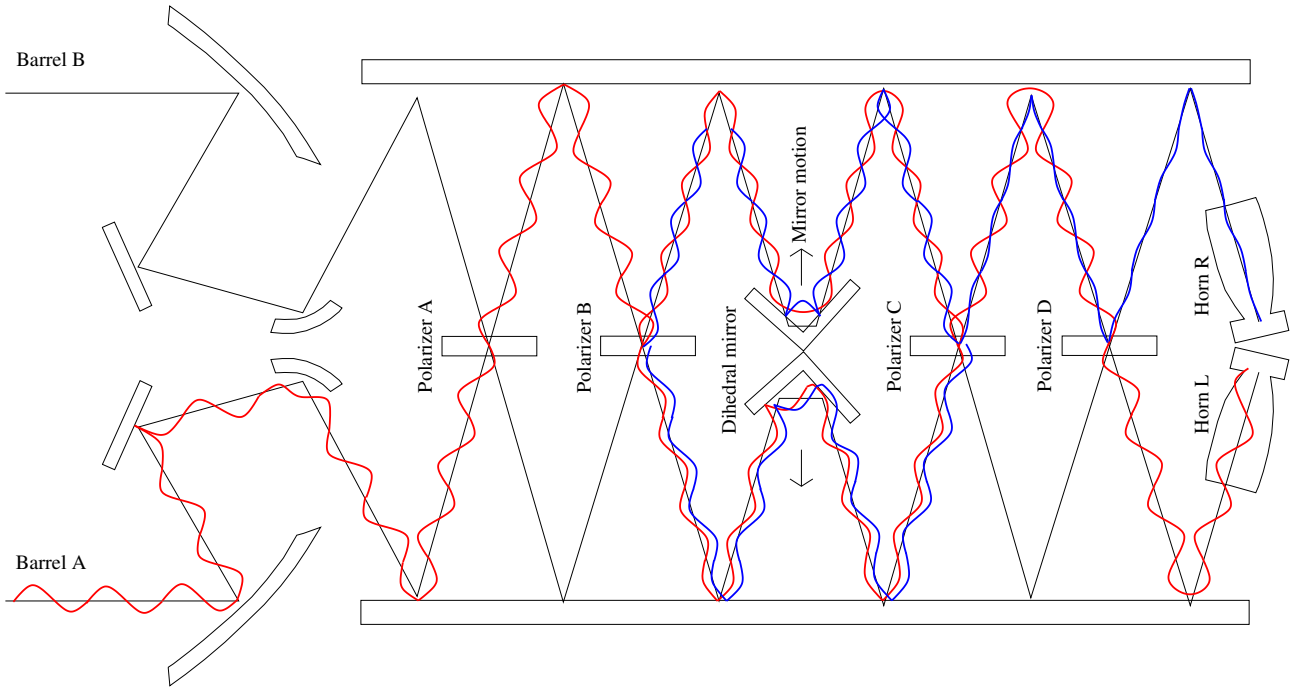

Figure 1: PIXIE optics example. Monochromatic pure vertical polarization (red) enters barrel A at the left side of the figure. It passes through the vertical polarizer A unmolested, but is split into two different linear combinations of vertical and horizontal (blue) polarization at the diagonal polarizer B. It then encounters the moving mirror, which in this example slightly retards the top optical path. The rays are combined in the next diagonal polarizer C, but due to the phase delay the horizontal polarization does not fully cancel. The vertical polarization is correspondingly lower. The final vertical polarizer (D) sends the vertical/horizontal polarization to horn L/R respectively. If the mirror displacement were zero, all radiation entering barrel A/B would end up in horn L/R.

In this paper we present a python-based time-ordered data simulator and map-maker for PIXIE, based on the mission concept proposed to NASA in 2016, and use them to make PIXIE spectral sky maps. We then use this framework to study the impact of some of the relevant systematic effects.

2 The PIXIE Fourier transform spectrometer

Unlike most CMB experiments, but like FIRAS, PIXIE does not use a large number of detectors and frequency filters to measure the frequency spectrum. Instead it splits the incoming radiation into two paths, introduces a variable delay between them, and then lets them interfere with each other. For each delay used, this results in a measurement of the radiation's autocorrelation function, which once mapped out can be Fourier transformed to recover the frequency spectrum. This indirect way of measuring the spectrum is called a Fourier transform spectrometer (FTS).

To improve the dynamic range PIXIE uses two FTSes (labeled "A" and "B" in the following) each with its own opening ("barrel") towards either the sky or a reference blackbody. The two barrels are collimated, and the interferometers are coupled in a total-intensity-nulling configuration. The situation is illustrated in figure 1.

The barrels are operated in one of two modes: In *single-barrel mode* one barrel is exposed to the sky while the other is covered by a 2.725 K calibrator (Kogut et al., 2011). This cancels the contribution from the CMB monopole, leaving the 3 orders of magnitude smaller dipole as the dominant signal. In *double-barrel mode* both barrels are exposed to the sky. In this case the entire total intensity signal is canceled, and only the much weaker polarization signal is left. In either case, the nulling greatly reduces the amplitude of the modulated signal that reaches the detectors. Many systematic effects are proportional to the total signal, and are therefore similarly reduced by this technique.

To be able to simulate PIXIE observations, we need to know how the power incident on its detectors relates to

the incoming radiation. This was done by Kogut et al. (2011), but is repeated here in more detail for convenience.

We can expand the electric field $\mathbf{E}^A(t)$, $\mathbf{E}^B(t)$ that enters PIXIE's barrels in terms of Jones vectors as

$$\begin{aligned}\mathbf{E}^A(t) &= \mathrm{Re}\int_0^\infty d\omega\Big(\tilde{E}_x^A(\omega)\mathbf{e}_x + \tilde{E}_y^A(\omega)\mathbf{e}_y\Big)e^{i(kz-\omega t)}\\ \mathbf{E}^B(t) &= \mathrm{Re}\int_0^\infty d\omega\Big(\tilde{E}_x^B(\omega)\mathbf{e}_x + \tilde{E}_y^B(\omega)\mathbf{e}_y\Big)e^{i(kz-\omega t)}\end{aligned} \tag{1}$$

where ω is the angular frequency of the radiaton and $\tilde{\mathbf{E}}^A(\omega)$ and $\tilde{\mathbf{E}}^B(\omega)$ are (complex) Jones vectors at that angular frequency.

After entering the barrels the light encounters polarizer A, which lets through vertical polarization and reflects horizontal[1]. After this, the Jones vectors in left (A) and right (B) shafts are

$$\tilde{\mathbf{E}}^{A1} = \tilde{E}_x^A\mathbf{e}_x + \tilde{E}_y^B\mathbf{e}_y \qquad\qquad \tilde{\mathbf{E}}^{B1} = \tilde{E}_x^B\mathbf{e}_x + \tilde{E}_y^A\mathbf{e}_y \tag{2}$$

After passing through the diagonal polarizer B, we have

$$\tilde{\mathbf{E}}^{A2} = \frac{1}{\sqrt{2}}[\tilde{E}_x^A + \tilde{E}_y^B]\mathbf{e}_a + \frac{1}{\sqrt{2}}[-\tilde{E}_x^B + \tilde{E}_y^A]\mathbf{e}_b \qquad \tilde{\mathbf{E}}^{B2} = \frac{1}{\sqrt{2}}[\tilde{E}_x^B + \tilde{E}_y^A]\mathbf{e}_a + \frac{1}{\sqrt{2}}[-\tilde{E}_x^A + \tilde{E}_y^B]\mathbf{e}_b \tag{3}$$

where $\mathbf{e}_a \equiv \frac{1}{\sqrt{2}}[\mathbf{e}_x + \mathbf{e}_y]$ and $\mathbf{e}_b \equiv \frac{1}{\sqrt{2}}[-\mathbf{e}_x + \mathbf{e}_y]$. The dihedral mirror then imparts a path length difference between the two sides, advancing A by $\frac{1}{2}\Delta t$ and retarding B by $\frac{1}{2}\Delta t$, which is achieved by multiplying A by $\delta^+ = e^{-\frac{1}{2}i\omega\Delta t}$ and B by $\delta^- = e^{\frac{1}{2}i\omega\Delta t}$:

$$\tilde{\mathbf{E}}^{A3} = \frac{\delta^+}{\sqrt{2}}[\tilde{E}_x^A + \tilde{E}_y^B]\mathbf{e}_a + \frac{\delta^+}{\sqrt{2}}[-\tilde{E}_x^B + \tilde{E}_y^A]\mathbf{e}_b \qquad \tilde{\mathbf{E}}^{B3} = \frac{\delta^-}{\sqrt{2}}[\tilde{E}_x^B + \tilde{E}_y^A]\mathbf{e}_a + \frac{\delta^-}{\sqrt{2}}[-\tilde{E}_x^A + \tilde{E}_y^B]\mathbf{e}_b \tag{4}$$

Polarizer C is also diagonal, resulting in

$$\tilde{\mathbf{E}}^{A4} = \frac{\delta^+}{\sqrt{2}}[\tilde{E}_x^A + \tilde{E}_y^B]\mathbf{e}_a + \frac{\delta^-}{\sqrt{2}}[-\tilde{E}_x^A + \tilde{E}_y^B]\mathbf{e}_b \qquad \tilde{\mathbf{E}}^{B4} = \frac{\delta^-}{\sqrt{2}}[\tilde{E}_x^B + \tilde{E}_y^A]\mathbf{e}_a + \frac{\delta^+}{\sqrt{2}}[-\tilde{E}_x^B + \tilde{E}_y^A]\mathbf{e}_b \tag{5}$$

And the final polarizer D is vertical. The output of this enters the left (L) and right (R) feedhorns.

$$\begin{aligned}\tilde{\mathbf{E}}^L = \tilde{\mathbf{E}}^{A5} &= \frac{1}{2}\Big[\delta^+(\tilde{E}_x^A + \tilde{E}_y^B) + \delta^-(\tilde{E}_x^A - \tilde{E}_y^B)\Big]\mathbf{e}_x + \frac{1}{2}\Big[\delta^-(\tilde{E}_x^B + \tilde{E}_y^A) + \delta^+(-\tilde{E}_x^B + \tilde{E}_y^A)\Big]\mathbf{e}_y\\ &= \big[\tilde{E}_x^A\cos(\omega\Delta t/2) - i\tilde{E}_y^B\sin(\omega\Delta t/2)\big]\mathbf{e}_x + \big[\tilde{E}_y^A\cos(\omega\Delta t/2) + i\tilde{E}_x^B\sin(\omega\Delta t/2)\big]\mathbf{e}_y \qquad (6)\\ \tilde{\mathbf{E}}^R = \tilde{\mathbf{E}}^{B5} &= \frac{1}{2}\Big[\delta^-(\tilde{E}_x^B + \tilde{E}_y^A) + \delta^+(\tilde{E}_x^B - \tilde{E}_y^A)\Big]\mathbf{e}_x + \frac{1}{2}\Big[\delta^+(\tilde{E}_x^A + \tilde{E}_y^B) + \delta^-(-\tilde{E}_x^A + \tilde{E}_y^B)\Big]\mathbf{e}_y\\ &= \big[\tilde{E}_x^B\cos(\omega\Delta t/2) + i\tilde{E}_y^A\sin(\omega\Delta t/2)\big]\mathbf{e}_x + \big[\tilde{E}_y^B\cos(\omega\Delta t/2) - i\tilde{E}_x^A\sin(\omega\Delta t/2)\big]\mathbf{e}_y \qquad (7)\end{aligned}$$

2.1 Stokes parameters

After passing through all this, the light enters the feedhorns and hits the detectors. The power deposited here can be decomposed into Stokes parameters[2]

$$\tilde{I} = \langle|\tilde{E}_x|^2\rangle + \langle|\tilde{E}_y|^2\rangle \qquad \tilde{Q} = \langle|\tilde{E}_x|^2\rangle - \langle|\tilde{E}_y|^2\rangle \qquad \tilde{U} = 2\,\mathrm{Re}\langle\tilde{E}_x\tilde{E}_y^*\rangle \qquad \tilde{V} = -2\,\mathrm{Im}\langle\tilde{E}_x\tilde{E}_y^*\rangle \tag{8}$$

[1] Before this it encounters the primary mirror, folding flats, secondary mirror, and transfer mirror 1, but these lead to the same phase shifts on both the A and B side optical paths, so they can be neglected.

[2] The quantities with tildes are for a single plane wave. The full Stokes parameters are obtained by integrating these. E.g. $I(\Delta t) = \int_0^\infty \tilde{I}(\omega)d\omega$.

so we need to evaluate $P_{xx} = \langle|\tilde{E}_x|^2\rangle$, $P_{yy} = \langle|\tilde{E}_y|^2\rangle$ and $P_{xy} = \langle\tilde{E}_x\tilde{E}_y^*\rangle$. For the left horn[3] we get

$$\begin{aligned}
P^L_{xx} &= \langle\tilde{E}^L_x\tilde{E}^{L*}_x\rangle \\
&= \frac{1}{2}\big[1+\cos(\omega\Delta t)\big]\langle\tilde{E}^A_x\tilde{E}^{A*}_x\rangle + \frac{1}{2}\big[1-\cos(\omega\Delta t)\big]\langle\tilde{E}^B_y\tilde{E}^{B*}_y\rangle - \frac{i}{2}\langle\tilde{E}^A_x\tilde{E}^{B*}_y + \tilde{E}^{A*}_x\tilde{E}^B_y\rangle\sin(\omega\Delta t) \\
&= \frac{1}{4}\big[\tilde{I}^A + \tilde{I}^B + \tilde{Q}^A - \tilde{Q}^B + (\tilde{I}^A - \tilde{I}^B + \tilde{Q}^A + \tilde{Q}^B)\cos(\omega\Delta t) - 4\,\mathrm{Im}(\tilde{E}^A_x\tilde{E}^{B*}_y)\sin(\omega\Delta t)\big] \qquad (9)\\
P^L_{yy} &= \frac{1}{4}\big[\tilde{I}^B + \tilde{I}^A + \tilde{Q}^B - \tilde{Q}^A - (\tilde{I}^B - \tilde{I}^A + \tilde{Q}^B + \tilde{Q}^A)\cos(\omega\Delta t) - 4\,\mathrm{Im}\langle\tilde{E}^B_x\tilde{E}^{A*}_y\rangle\sin(\omega\Delta t)\big] \qquad (10)\\
P^L_{xy} &= \frac{1}{4}\big[\tilde{U}^A - \tilde{U}^B - i\tilde{V}^A - i\tilde{V}^B + (\tilde{U}^A + \tilde{U}^B - i\tilde{V}^A + i\tilde{V}^B)\cos(\omega\Delta t) + 2i\langle\tilde{E}^A_x\tilde{E}^{B*}_x + \tilde{E}^B_y\tilde{E}^{A*}_y\rangle\sin(\omega\Delta t) \qquad (11)
\end{aligned}$$

Hence

$$\begin{aligned}
\tilde{I}^L &= \frac{1}{2}\big[\tilde{I}^A + \tilde{I}^B + (\tilde{I}^A - \tilde{I}^B)\cos(\omega\Delta t) - 2\,\mathrm{Im}\langle\tilde{E}^A_x\tilde{E}^{B*}_y + \tilde{E}^B_x\tilde{E}^{A*}_y\rangle\sin(\omega\Delta t)\big] \\
\tilde{Q}^L &= \frac{1}{2}\big[\tilde{Q}^A - \tilde{Q}^B + (\tilde{Q}^A + \tilde{Q}^B)\cos(\omega\Delta t) - 2\,\mathrm{Im}\langle\tilde{E}^A_x\tilde{E}^{B*}_y - \tilde{E}^B_x\tilde{E}^{A*}_y\rangle\sin(\omega\Delta t)\big] \\
\tilde{U}^L &= \frac{1}{2}\big[\tilde{U}^A - \tilde{U}^B + (\tilde{U}^A + \tilde{U}^B)\cos(\omega\Delta t) - 2\,\mathrm{Im}\langle\tilde{E}^A_x\tilde{E}^{B*}_x + \tilde{E}^B_y\tilde{E}^{A*}_y\rangle\sin(\omega\Delta t)\big] \\
\tilde{V}^L &= \frac{1}{2}\big[\tilde{V}^A + \tilde{V}^B + (\tilde{V}^A - \tilde{V}^B)\cos(\omega\Delta t) - 2\,\mathrm{Re}\langle\tilde{E}^A_x\tilde{E}^{B*}_x + \tilde{E}^B_y\tilde{E}^{A*}_y\rangle\sin(\omega\Delta t)\big] \qquad (12)
\end{aligned}$$

The value of the barrel cross-terms depends on whether PIXIE is in single or double barrel mode.

Single barrel mode In single barrel mode only one barrel is exposed to the sky; the other one observes a static calibrator object. The light entering the two barrels is therefore uncorrelated, and all the cross-terms disappear.

$$\begin{aligned}
\tilde{I}^L &= \frac{1}{2}\big[\tilde{I}^A + \tilde{I}^B + (\tilde{I}^A - \tilde{I}^B)\cos(\omega\Delta t)\big] & \tilde{Q}^L &= \frac{1}{2}\big[\tilde{Q}^A - \tilde{Q}^B + (\tilde{Q}^A + \tilde{Q}^B)\cos(\omega\Delta t)\big] \\
\tilde{V}^L &= \frac{1}{2}\big[\tilde{V}^A + \tilde{V}^B + (\tilde{V}^A - \tilde{V}^B)\cos(\omega\Delta t)\big] & \tilde{U}^L &= \frac{1}{2}\big[\tilde{U}^A - \tilde{U}^B + (\tilde{U}^A + \tilde{U}^B)\cos(\omega\Delta t)\big] \qquad (13)
\end{aligned}$$

Double barrel mode In double barrel mode the two barrels are both coaligned and exposed to the sky, so they observe the same wavefront entering. As PIXIE's angular resolution is not infinite it is sensitive to wavefronts that are off-axis by a few degrees, causing the two barrels to act as a 2-element spatial interferometer. Light arriving from a single direction $\hat{n}$ will hit Barrel B a time $\tau = \hat{n}\cdot\mathbf{b}/c$ before barrel A, where $\mathbf{b}$ is the distance vector from barrel A to barrel B, and c is the speed of light (see Nagler et al. (2015, appendix)). So in this case $\tilde{\mathbf{E}}^B = \gamma\tilde{\mathbf{E}}^A$ with $\gamma = e^{-i\omega\tau}$.

$$\begin{aligned}
\tilde{I}^L &= \tilde{I}^A + \tilde{V}^A\cos(\omega\tau)\sin(\omega\Delta t) & \tilde{Q}^L &= \tilde{Q}^A\cos(\omega\Delta t) - \tilde{U}^A\sin(\omega\tau)\sin(\omega\Delta t) \\
\tilde{V}^L &= \tilde{V}^A - I^A\cos(\omega\tau)\sin(\omega\Delta t) & \tilde{U}^L &= \tilde{U}^A\cos(\omega\Delta t) - \tilde{Q}^A\sin(\omega\tau)\sin(\omega\Delta t) \qquad (14)
\end{aligned}$$

The total signal will be the contribution from all directions integrated over the barrel beam. The cross terms (those proportional to $\sin(\omega\Delta t)$ are antisymmetric with respect to the baseline $\mathbf{b}$ separating the two barrels, making it cancel to first order when integrated over the symmetric beam. Furthermore, the $\sin(\omega\Delta t)$ dependence of any residual is anti-symmetric with respect to the mirror stroke, forcing these terms into the (unphysical) imaginary part of the frequency maps. This imaginary part contains none of the real signal and would usually be discarded, but can be inspected as a test for systematic errors.

If the barrels are not perfectly collimated, or if they have asymmetric sidelobes or different beam size, then the situation will be more complicated, as only part of the radiation that enters the barrels will be correlated.

These cross terms are not implemented in the current version of the simulator, but for the reasons above we do not expect this to impact our results meaningfully.

In the absence of the cross terms terms, the signal in double barrel mode is identical to that of single barrel mode with $(I^A, Q^A, U^A, V^A) = (I^B, Q^B, U^B, V^B)$, so we can use the single barrel eqs (13) in the following without further loss of generality.

A fuller treatment of the effects of beam asymmetries can be found in Kogut & Fixsen (2018).

[3]The right horn follows by symmetry: $(L, A, B) \leftrightarrow (R, B, A)$.

2.2 Detector response

PIXIE has an x and y-oriented detector in each horn. The power deposited on each of these is

$$\begin{aligned}
s_x^L(\Delta t) &= \frac{1}{4}\int_0^\infty \Big(\tilde{I}^A + \tilde{I}^B + \tilde{Q}^A - \tilde{Q}^B + (\tilde{I}^A - \tilde{I}^B + \tilde{Q}^A + \tilde{Q}^B)\cos(\omega\Delta t)\Big)d\omega \\
&= \frac{1}{4}\big[I^A + I^B + Q^A - Q^B\big]_0 + \frac{1}{4}\big[I^A - I^B + Q^A + Q^B\big]_{\Delta t} \\
s_y^L(\Delta t) &= \frac{1}{4}\big[I^B + I^A + Q^B - Q^A\big]_0 - \frac{1}{4}\big[I^B - I^A + Q^B + Q^A\big]_{\Delta t} \\
s_x^R(\Delta t) &= \frac{1}{4}\big[I^B + I^A + Q^B - Q^A\big]_0 + \frac{1}{4}\big[I^B - I^A + Q^B + Q^A\big]_{\Delta t} \\
s_y^R(\Delta t) &= \frac{1}{4}\big[I^A + I^B + Q^A - Q^B\big]_0 - \frac{1}{4}\big[I^A - I^B + Q^A + Q^B\big]_{\Delta t}
\end{aligned} \tag{15}$$

where all the quantities depend on Δt and potentially τ, and where these are total Stokes parameters, not the per-frequency ones, e.g. $I = \int_0^\infty \tilde{I}(\omega)d\omega$, and $[\ldots]_{\Delta t}$ means that the quantities within should be evaluated at the time delay in the subscript.

Combining this with the effect of PIXIE's pointing on the sky, we can express the total detector response as a function of the sky autocorrelation functions.

$$\mathbf{s}^{\rm det}(t) = \overbrace{\frac{1}{2}\begin{bmatrix} \mathbf{e}_I + \mathbf{e}_Q & 0 \\ \mathbf{e}_I - \mathbf{e}_Q & 0 \\ 0 & \mathbf{e}_I + \mathbf{e}_Q \\ 0 & \mathbf{e}_I - \mathbf{e}_Q \end{bmatrix}}^{\text{Detector response}} \cdot \overbrace{\frac{1}{2}\begin{bmatrix} 1 & M & 1 & -M \\ M & 1 & -M & 1 \end{bmatrix}}^{\text{Horn response}} \cdot \overbrace{\begin{bmatrix} R_{1t}\cdot \mathbf{s}_A^{\rm sky}(\hat{p}_{1t}, 0) \\ R_{2t}\cdot \mathbf{s}_B^{\rm sky}(\hat{p}_{2t}, 0) \\ R_{1t}\cdot \mathbf{s}_A^{\rm sky}(\hat{p}_{1t}, \Delta t) \\ R_{2t}\cdot \mathbf{s}_B^{\rm sky}(\hat{p}_{2t}, \Delta t) \end{bmatrix}}^{\text{Barrel signal}} \tag{16}$$

$\mathbf{s}^{\rm det}(t) = [s_x^L, s_y^L, s_x^R, s_y^R]$ is the vector of detector responses at time t, $\hat{p}_{bt}$ is the sky pointing of barrel b at time t, $\mathbf{s}_b^{\rm sky}(\hat{p}, \Delta t)$ is the beam-smoothed, frequency-weighted sky autocorrelation function Stokes vectors for the given pointing and time delay as seen by barrel b (different barrels can see different skies because one barrel may be covered by a blackbody calibrator), R_{bt} is a matrix that rotates the polarization basis from sky to instrument coordinates, $M = \mathrm{diag}(1, -1, -1, 1)$ is a matrix that flips the sign of linear polarization, and $\mathbf{e}_I = (1, 0, 0, 0)$ and $\mathbf{e}_Q = (0, 1, 0, 0)$ are Stokes I and Q basis vectors. PIXIE's interferometry shows up in two ways here: The sky autocorrelation function, rather than just its intensity, is what is measured; and the barrel signal differencing in the horn response.

2.3 Readout

Of course, a real instrument does not read out data with infinite time resolution, but as a set of discrete samples, each of which is noisy. The PIXIE hardware will also apply a bandpass filter to avoid aliasing and suppress low-frequency noise. Taking this into account, we model the time-ordered data as

$$\mathbf{d}_i = B_{ij}\int_{t_j-\Delta t/2}^{t_j+\Delta t/2} \mathbf{s}^{\rm det}(t)\mathrm{d}t + \mathbf{n}_i \tag{17}$$

where i is the sample index, B is the bandpass filter, Δt is the sample interval and $\mathbf{n}_i$ is the noise in sample i. We implement this sample integral by using Gaussian quadrature with $N_{\rm sub}$ sub-samples, with a typical value of $N_{\rm sub}$ being 9.

For the bandpass filter we used a Butterworth bandpass filter,

$$B(f) = \Big(1 + \Big[\frac{f}{0.01\mathrm{Hz}}\Big]^{-5}\Big)^{-1}\Big(1 + \Big[\frac{f}{100\mathrm{Hz}}\Big]^{5}\Big)^{-1}. \tag{18}$$

2.4 Frequency response

PIXIE's frequency response is limited above 1-2 THz by the roughness of the mirrors. Scattering from the mirrors provides a gradual decrease in the coupling of the detectors to the sky. The resulting apodized frequency response

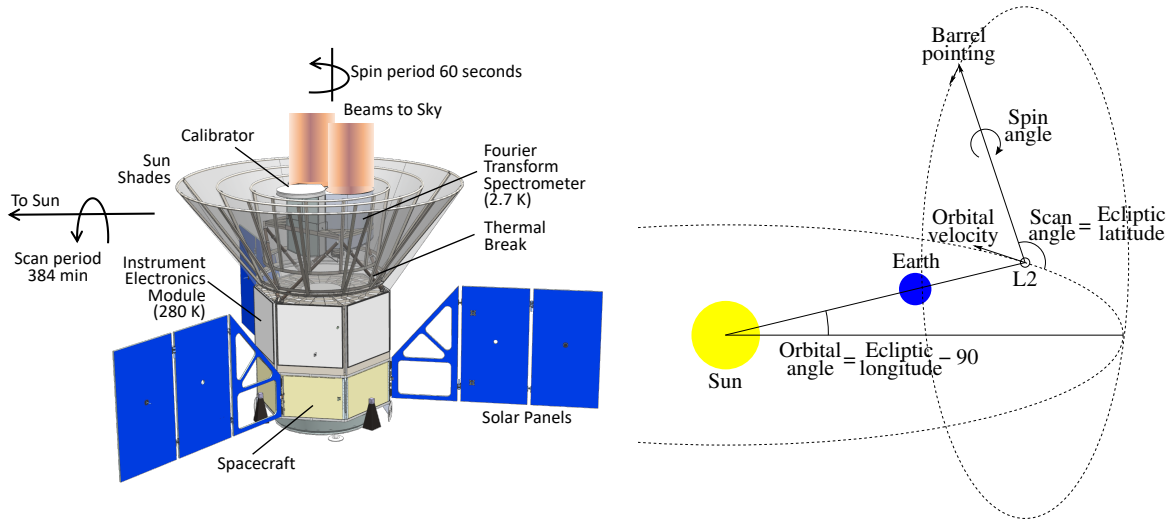

Figure 2: *Left*: The PIXIE observatory, showing the spin and scan axes relative to the barrel beams and the direction towards the sun. *Right*: PIXIE would be located at the Sun-Earth L2 point, and would scan in great circles while pointing 90° away from the Sun, adjusting its orientation stepwise between each scan. This results in the whole sky being covered every 6 months.

smoothly band-limits the signal to avoid aliasing from frequencies about the instrument's Nyquist frequency of 7 THz. Dispersion within the FTS from the finite spread of angles within the beam washes out the fringe amplitude at comparable frequencies. Synthesized channels at frequencies above ∼6 THz thus contain noise but no signal, providing a convenient check of the instrument noise.

We here model the total frequency response as $\rho(\nu) = e^{-\left[\frac{\nu}{1.5\,\mathrm{THz}}\right]^2}$.

3 Pointing

PIXIE would orbit at the Sun-Earth L2 point, placing it in the ecliptic, with a heliocentric ecliptic latitude $b = 0$ and longitude $l = l_0 + 360° \frac{t-t_0}{T_{\rm orbit}}$[4] with $T_{\rm orbit} = 1$ year. In addition to this orbital motion, PIXIE also scans great circles[5] perpendicular to the direction towards the sun, with a linearly increasing scan angle $\alpha_{\rm scan} = \alpha_{\rm scan,0} + 360° \frac{t-t_0}{T_{\rm scan}}$. To form an actual great circle the scan axis does not move continuously with b, but updates in steps after each circle has been completed: $\alpha_{\rm orbit} = l_0 + 360° \left\lfloor \frac{t-t_0}{T_{\rm scan}} \right\rfloor \frac{T_{\rm scan}}{T_{\rm orbit}}$. On top of this scanning motion, the telescope also spins rapidly around the barrel boresight in order to modulate the observed polarization and reject systematics: $\alpha_{\rm spin} = \alpha_{\rm spin,0} + 360° \frac{t-t_0}{T_{\rm spin}}$. And finally, while it is spinning the dihedral mirror sweeps backwards and forwards at constant speed, varying the path length time difference in the Fourier transform spectrometer by $\Delta t = A_{\rm delay}\,\mathrm{triangle}\left(\frac{t-t_0}{T_{\rm stroke}}\right)$, with $A_{\rm delay} = 10.40303\mathrm{mm}/c$ for the purposes of this paper, but varying somewhat by observing mode in the real experiment, and with triangle(x) being the triangle wave with period 1, mean 0 and a zero crossing at $x = 0$.

To allow PIXIE mapmaking to use fast Fourier transform methods, the stroke, spin and scan periods will be synchronized such that there is an integer number of strokes in a spin, and an integer number of spins in a scan. We will use the values $T_{\rm spin} = 60$s, $T_{\rm stroke} = T_{\rm spin}/8 = 7.5$ sec, $T_{\rm scan} = 384 T_{\rm spin} = 384$ min here. The time-ordered data (TOD) simulator purposefully does not depend on integer ratios to be able to investigate the consequences of small deviations from integer ratios.

To summarize, PIXIE moves in four different ways: It orbits with a 1 year period; it scans in great circles perpendicular to the direction towards the sun with a 384 minute period; it spins around the boresight with a

[4] We're ignoring the orbital eccentricity here for simplicity, but nothing in the simulation or mapmaking relies on the longitude changing at a constant rate, so it would be trivial to add support for eccentricity.

[5] Getting sufficient sun shielding might require the opening angle of the scan to be smaller than 180°. This would make the scans small circles instead. This would result in 1. the ecliptic poles no longer being covered, and 2. the `add_to_sky` operation in section 6.5 would be somewhat more complicated. Aside from that, nothing changes.

1 minute period; and it strokes the FTS mirror with a 7.5 second period. Aside from the orbital period these numbers are subject to change, but the period ratios will be kept at integer numbers.

In order to speed up our simulations we will modify the scanning pattern we simulate in one important respect. The actual L2 orbital period given above results in about 1370 scans per orbit, which results in 7.6 scans per PIXIE beam FWHM on the equator after half an orbit. We avoid this oversampling by simulating a faster $T_{\rm orbit} = 384 T_{\rm scan}$.

A barrel-to-sky rotation matrix that implements this pointing model is

$$R_{\rm tot}(b,t) = R_{\rm orient}(t) R_{\rm barrel}(b) \tag{19}$$

$$R_{\rm orient}(t) = R_z\big(\alpha_{\rm orbit}(t)\big) R_y\Big(\frac{\pi}{2} - \alpha_{\rm eclip}\Big) R_z\big(\alpha_{\rm scan}(t)\big) R_y\Big(\frac{\pi}{2} - \alpha_{\rm open}\Big) R_z\big(\alpha_{\rm spin}(t)\big) \tag{20}$$

$$R_{\rm barrel}(b) = R_z\big(\Delta\phi(b)\big) R_y\big(\Delta\theta(b)\big) R_z\big(\Delta\psi(b)\big) \tag{21}$$

Here $R_{\rm barrel}(b)$ represents the orientation of barrel b relative to the spacecraft. Fiducially $R_{\rm barrel} = 1$ for both barrels, but we include this rotation to be able to support misaligned barrels or more complicated beams. $R_{\rm orient}(t)$ represents PIXIE's orientation in space at time t, and in addition to the angles described above includes $\alpha_{\rm eclip}$ and $\alpha_{\rm open}$, which represent the offset of PIXIE's orbital plane from the ecliptic and the opening angle offset (to support non-great-circle scans), both of which are fiducially 0. $R_y(\theta)$ and $R_z(\theta)$ are rotations around the y and z axes by an angle θ.[6]

$R_{\rm tot}$ encodes both the sky coordinates and polarization rotation,

$$x_i = R_{\rm tot,xi} \qquad y_i = R_{\rm tot,yi} \qquad p_i \equiv z_i = R_{\rm tot,zi} \tag{22}$$

$$l = \tan^{-1}(p_y/p_x) \qquad b = \tan^{-1}\Big(\frac{p_z}{\sqrt{p_x^2 + p_y^2}}\Big) \qquad \gamma = \tan^{-1}\Big(\frac{x_z}{p_y x_x - p_x x_y}\Big). \tag{23}$$

with all the above being a function of the barrel index and time. $\hat{p} = (p_x, p_y, p_z)$ is the pointing vector and γ is the polarization basis rotation, and corresponds to a Stokes rotation matrix

$$R_{\rm stok} = \begin{bmatrix} 1 & 0 & 0 & 0 \\ 0 & \cos(2\gamma) & -\sin(2\gamma) & 0 \\ 0 & \sin(2\gamma) & \cos(2\gamma) & 0 \\ 0 & 0 & 0 & 1 \end{bmatrix} \tag{24}$$

4 Evaluating the sky autocorrelation function at the observed location

As PIXIE observes the sky it mesures the autocorrelation function of the radiation coming from the points it scans past. To simulate the PIXIE signal we therefore need to be able to evaluate the I, Q and U autocorrelation functions [7] at an arbitrary point $\hat{p}$ on the sky for an arbitrary phase delay Δt for each component that makes up the sky (CMB, dust, etc.).

4.1 Precomputing the autocorrelation function as a data cube

A straightforward and general way of doing this would be to precompute the full-sky autocorrelation function:

1. Evaluate the full-sky spectrum at equi-spaced frequencies
2. Apply any frequency-dependent beam to each frequency map and scale each frequency by the instrument's frequency response.
3. Fourier transform the result to get a (pixelized version of) the full-sky autocorrelation function.
4. Apply any mirror-position-dependent beam or response to each delay in the result.

[6] In ecliptic coordinates z represents the zenith and x the zero longitude direction. In barrel coordinates, z represents the fiducial barrel pointing.

[7] We're ignoring V polarization here. See section 2.1.

To read off the value at a general $(\hat{p}, \Delta t)$ one would then do an interpolated lookup in this $N_{\rm pix}$ by $N_{\rm delay}$ data cube. This approach has the advantage of being able to handle both frequency- and delay-dependent beams, which are otherwise hard to implement.

However, it also has some important limitations. Because it stores the full spectrum/autocorrelation function in each pixel, its memory requirements scale poorly with resolution. This makes it impractical to investigate the effect of sub-resolution features (both spectrally and spatially) - to do so would require the data cube to be pixelized at many times higher resolution than the PIXIE output map, which would make the memory requirements of this approach prohibitively high. For example, for 0.1° spatial resolution and 5000 frequency bins, storing the full-sky autocorrelation function would need about 700 GB of RAM.

We will therefore save the data cube approach for a future investigation of the effects of frequency- and delay-dependent beams, and use an approach that allows for high-resolution simulations in this paper.

4.2 Other approaches

If one assumes a frequency-independent beam, which should be a good approximation for PIXIE, and if the spectrum can be written as a linear sum of a smaller number of spatial templates, then it's sufficient to apply the beam to those templates rather than the spectrum itself. This decouples the spatial and spectral dimensions, making it possible to evaluate the spectrum in one pixel independently of the rest of the sky.

With this, we could imagine the following approach: For each sample, interpolate the spectrum parameters at $\hat{p}$, then evaluate the whole spectrum, apply the frequency response, Fourier transform it, and interpolate the value for Δt. In our example above, this would reduce the RAM requirements by a factor of 5000. But it would introduce another prohibitive cost: The need to evaluate the spectrum at thousands of frequencies and Fourier transform these for every sample in the TOD.[8]

4.3 Autocorrelation by Taylor expansion

In the end, we went for a Taylor expansion approach: The autocorrelation function is evaluated as a perturbation around a different but similar precomputed autocorrelation function. This is done differently for each sky component.

4.3.1 CMB

Taking into account the instrument's frequency response $\rho(\nu)$ (see section 2.4), PIXIE observes the CMB with the spectrum

$$I^{\rm CMB}_{\nu,I}(\hat{p},\nu) = \rho(\nu) B_\nu(\nu, T(\hat{p})) = \frac{2h\nu^3\rho(\nu)}{c^2} \frac{1}{e^{\frac{h\nu}{k_B T(\hat{p})}} - 1}. \tag{25}$$

Here the I subscript indicates the Stokes intensity parameter, and $T(\hat{p})$ is the CMB temperature at pointing $\hat{p}$. k_B and h are the Boltzmann and Planck constants respectively. Including the Doppler dipole, T only has a contrast of order 10^{-3}, so a Taylor expansion in T will converge rapidly. Our goal is $< 10^{-9}$ relative error, so an expansion to 3rd order, which should give order 10^{-12} error, should be sufficient. The expansion is

$$I^{\rm CMB}_{\nu,I}(\hat{p},\nu) = f_0(\nu) + f_1(\nu)\Delta T + \frac{1}{2} f_2(\nu)\Delta T^2 + \frac{1}{6} f_3(\nu)\Delta T^3 \tag{26}$$

where

$$\begin{aligned}
f_0 &= p(g_0 - 1)^{-1} & g_0 &= e^{a/T_0} \\
f_1 &= p f_0^2 g_1 & g_1 &= -g_0 a/T_0^2 \\
f_2 &= p(-2 f_0 f_1 g_1 - f_0^2 g_2) & g_2 &= a(2g_0 - T_0 g_1)/T_0^3 \\
f_3 &= p(-2 f_1^2 g_1 - 2 f_0 f_2 g_1 - 4 f_0 f_1 g_2 - f_0^2 g_3) & g_3 &= -(3/T_0 + a/T_0^2) g_2 + a g_1/T_0^3
\end{aligned}$$

[8] A hybrid approach between these two would be to precompute the autocorrelation function for a chunk of the sky around the current sample, and reuse that for subsequent samples until a sample falls outside the chunk, and then precompute a new chunk. We investigated this in the hopes of being able to support frequency-dependent beams, but found that edge effects and the flat-sky-approximation needed to perform beam-smoothing on a small patch did not result in the required accuracy. This may still be a good approach for frequency-independent beam simulations, though.

and where $p = \frac{2h\nu^3\rho(\nu)}{c^2}$, $a = h\nu/k_B$ and $\Delta T(\hat{p}) = T(\hat{p}) - T_0$ with $T_0 = 2.725$K.

The autocorrelation function is simply the cosine transform[9] of the spectral power density,

$$I_{\Delta t}(\Delta t) = \int_0^\infty I_\nu(\nu)\cos(2\pi\nu\Delta t)d\nu \equiv \bar{I}_\nu(\Delta t). \tag{27}$$

where $\bar{x}$ indicates the cosine transform of x. Applying this to the Taylor expansion, we get

$$I^{\rm CMB}_{\Delta t,I}(\hat{p},\Delta t) = \bar{f}_0(\Delta t) + \bar{f}_1(\Delta t)\Delta T + \frac{1}{2}\bar{f}_2(\Delta t)\Delta T^2 + \frac{1}{6}\bar{f}_3(\Delta t)\Delta T^3 \tag{28}$$

Hence, we can compute the autocorrelation for any $\hat{p}, \Delta t$ if we simply precompute the four position-independent functions $\{f_i\}$.[10] Evaluating the CMB autocorrelation at $(\hat{p}, \Delta t)$ is hence reduced to being able to evaluate a sampled version of $\{f_i\}$ at (non-sample) position Δt and the full-sky pixelized map ΔT at (non-pixel) position $\hat{p}$. We perform both of these using (bi-)cubic spline interpolation from `numpy.ndimage.map_coordinates`.

The CMB has frequency-independent polarization, so the Q, U autocorrelation functions can be derived from I by scaling them by the local Q, U polarization fractions. I.e. $I^{\rm CMB}_{\Delta t,Q|U}(\hat{p},\Delta t) = I^{\rm CMB}_{\Delta t,I}(\hat{p},\Delta t)\frac{I^{\rm CMB}_{{\rm ref},Q|U}(\hat{p})}{I^{\rm CMB}_{{\rm ref},I}(\hat{p})}$.

The input CMB map $\Delta T, Q, U$ was simulated by drawing random, Gaussian T,E,B and ϕ spherical harmonics coefficients from a typical CMB power spectrum as output by CAMB[11] and projecting them on a sky with 0.1° pixels in equirectangular (CAR) projection using the `libsharp` Spherical Harmonics Transform library (Reinecke & Seljebotn, 2013). The lensing potential ϕ was then used to lens the T, Q and U maps. We then added the 2.725 K CMB monopole to the T component before Doppler boosting the sky[12] to account for our motion relative to the CMB, resulting in the CMB dipole.

4.3.2 Dust

We model the dust as a modified blackbody with constant $T_D = 19.6$K and $\beta = 1.59$, but varying opacity. The observed spectrum is thus

$$I^{\rm dust}_{\nu,i}(\hat{p},\nu) = A_i(\hat{p})\frac{h\nu^{3+\beta}\rho(\nu)}{c^2}\frac{1}{e^{\frac{h\nu}{k_B T_D}} - 1} \equiv A_i(\hat{p})f_{0\beta}(\nu) \tag{29}$$

for $i \in \{I, Q, U\}$. Here the prefactor $A_i(\hat{p})$ encodes the position-dependent dust opacity and polarization. Since T and β are constant, the frequency-dependent part of this spectrum is already position-independent, so we don't actually need to Taylor-expand in this case. We just need to precompute a single autocorrelation shape which is rescaled for each pointing.

$$I^{\rm dust}_{\Delta t,i}(\hat{p},\Delta t) = A_i(\hat{p})\bar{f}_{0\beta}(\Delta t). \tag{30}$$

This will need to be modified for more complicated dust models. If T_D or β only change slightly, then the Taylor expansion approach can be used. For more substantial variation, a better approach may be to model it as several dust components, each with fixed parameters.

The input dust map was simulated using the Python Sky Model Thorne et al. (2017) code `PySM` of a thermal dust-only sky evaluated at 600 GHz (with no bandpass). This was computed at HEALPix $N_{\rm side} = 512$, but the polarization map `PySM` produces is limited to 2° resolution due to the limited resolution of the Planck polarized dust maps it uses as input. This HEALPix map was then repixelized to 0.1° equirectangular (CAR) pixelization in ecliptic coordinates by computing its spherical harmonics coefficients, projecting these onto CAR, and then rotating from galactic to ecliptic coordinates using bicubic spline interpolation and rotating the polarization vectors to compensate.

4.3.3 Other components

The results reported here are based on simulations that only include CMB and dust, but other components such as synchrotron, free-free, CO, AME, etc. can be implemented in a similar vein as above, as long as they can be approximated as a sum of constant-spectral-shape components or can be Taylor-expanded to sufficient accuracy.

[9] We implemented the cosine transform using a discrete cosine transform with a sample interval of 0.5 GHz and a max frequency of 6.8 THz.

[10] If we had not needed to support the frequency response of the instrument, we could have avoided the Taylor expansion by absorbing variation in T into rescaling of v. Sadly, PIXIE has significant damping at high frequency, so this approach does not work.

[11] The spectrum used is provided in the file `inputs/cl_lensinput.dat`.

[12] $\beta = 0.0012301$ towards ecliptic coordinates $l = 171.646$, $b = -11.141$.

5 Beams and sidelobes

PIXIE will use multi-moded optics, as opposed to the single-moded optics common to many imaging CMB instruments. For a single-moded system, the number of modes is fixed at unity and the beam size depends on the etendue and observing wavelength ($\Omega \propto \lambda^2$). For a multi-moded system, the beam size is fixed and the number of modes depends on the etendue and wavelength ($N_{\rm modes} \propto \Omega/\lambda^2$). This has been tested in the lab for PIXIE, and the beam was found to be *frequency-independent* above about 30 GHz (Kogut et al., 2015; Kogut & Fixsen, 2018). PIXIE's beam is also approximately top-hat shaped, but we will here approximate it with a Gaussian with FWHM of 1.9°.

As discussed in section 4.1, a frequency-independent beam is much cheaper to implement than a frequency-dependent one as long as the spectrum maps are linear functions of a small number of input maps. For our dust model this is simple - the spectrum is proportional to a single spatially varying dust opacity map, so it is sufficient to apply the beam to that map.

5.1 A small error in the CMB beam treatment

The CMB, on the other hand, is modeled as a 4th order Taylor expansion in ΔT, so in this case we should smooth each power of ΔT individually. We currently *do not do this*. Instead, we simply smooth the input ΔT, as one usually does when simulating CMB maps. This reduces the accuracy of our Taylor expansion, and should be fixed in a future release. However, this is not as serious as one might fear.

1. The main reason why we go to 4th order is the $O(10^{-3})$ CMB dipole, but the dipole is practically unaffected by the beam. The beam-relevant scales are much lower, at $O(10^{-5})$. The first incorrect correction term is the second order, which is down by another such factor, giving a relative accuracy of 10^{-5} for T, E and B perturbations. This is dwarfed by cosmic variance and noise for all PIXIE scales.

2. The same beam incorrect smoothing is used when evaluating the accuracy of the recovered maps. These errors therefore cancel, and the difference maps and error plots in the results section are identical to those we would have gotten if this error had not been made.

5.2 Sidelobes and asymmetric beams

So far we've assumed that the beam is isotropic and position-independent, so it can be implemented by a one-time smoothing of the maps. A full implementation of general beam shapes would be very expensive, as it requires an integral over (part of) the sky for every sample generated. However, we can capture all the interesting effects of complicated beams by expanding them as a series of symmetric beams with different pointing offsets. For example, a slightly elliptical beam can be approximated as the sum of two slightly offset symmetric beams. We implement this by replacing every evaluation of the sky autocorrelation function with a sum over such evaluations for each beam component. Each such beam component is defined by specifying $\Delta\phi$ and $\Delta\theta$ (see eq. (21)), a beam profile, and a Muller matrix which encodes its intensity and leakage properties.

5.3 Simulator pseudo-python

The full source code of the simulator can be found in the classes `OpticsSim` and `ReadoutSim` in `pixie.py` in `https://github.com/amaurea/pixie`, but the overall logic is summarized in the pseudo-code below.

```
for each barrel, beam:
    skies[barrel.sky, beam] = prepare_sky(barrel.sky, beam)
# Time-ordered data is generated and output in units of scans
for each scan:
    tod = zeros([ndet,nsamp*nsub])
    for each subsample in scan:
        elements = calc_orbital_parameters(subsample)
        for each detector:
            for each beam seen through each barrel by detector:
                p   = calc_pointing(elements, beam)
                sky = skies[barrel.sky, beam]
```

```
            # Compute the autocorrelation function at both
            # dt=0 (DC) and dt=p.delay (offset)
            sky_signal   = calc_sky_autocorr(sky, p)
            # Compute detector response to DC and offset sky Stokes parameters
            det_response = calc_det_response(det, barrel, p)
            tod[det,subsample] = calc_det_signal(sky_signal, det_response)
    # This uses Gaussian quadrature to integrate the subsamples
    # in each sample (so the subsamples are not equi-spaced)
    tod = downsample(tod, nsub)
    output(tod)
```

6 PIXIE map-making

6.1 Assumptions

PIXIE's observing strategy is designed to make mapmaking fast and accurate. To be as general as possible we avoided depending on these features in the TOD simulator, but we make use of them in the map-maker.

No DC signal The unmodulated component (DC) of the signal changes on minute timescales, which will not be recoverable due to correlated noise and the TOD highpass filter. We ignore this component in the map-maker, and simply treat it as a part of the noise.

Single sky We assume that the calibrator in single barrel mode is constant and unpolarized. That means that its effect can be taken into account simply by adding back the calibrator spectrum in map space, and the map-maker itself can ignore it, and set $\mathbf{s}_B^{\rm sky} = 0$. We also assume that the sky itself is time-independent, so there is just a single sky to solve for. Any deviations from this will be interpreted as noise.

In double barrel mode we assume that the two barrels see the same signal, and that the V and U antisymmetric leakage terms can be ignored. Since I can't be recovered in double barrel mode, the two barrels are equivalent to a single barrel with no I but twice the polarization signal, so we can again set $\mathbf{s}_B^{\rm sky} = 0$ as long as we multiply the detector response by 2. With this, equation (16) simplifies to

$$\mathbf{s}^{\rm det}(t) = G \cdot R_{\rm spin}(t) \cdot \mathbf{s}^{\rm sky}(\hat{p}_t, \Delta t) \tag{31}$$

where G is the detector-barrel response matrix $G = \frac{g}{4}[\mathbf{e}_I + \mathbf{e}_Q, \mathbf{e}_I - \mathbf{e}_Q, -\mathbf{e}_I + \mathbf{e}_Q, -\mathbf{e}_I - \mathbf{e}_Q]$ and $g = 1$ in single barrel mode and $g = 2$ in double barrel mode.

Regular scanning pattern PIXIE scans in great circles (rings) that pass through the ecliptic poles, and both barrels are perfectly aligned. This means that the scanning motion does not induce polarization rotation in ecliptic coordinates, and that all samples in a ring will have constant ecliptic longitude, up to pole wrapping. The sampling rate and telescope scan, spin and stroke speed are constant; and there is an integer number of samples per stroke, strokes per spin and spins per scan. Using this, the data model simplifies further to

$$\mathbf{s}_{ri}^{\rm sky} = G \cdot R_{\rm stok}\left(\frac{4\pi i}{N_{\rm spin}}\right) \cdot \mathbf{s}^{\rm sky}\left(\left[l = l_0 + r\Delta l, b = b_0 + \frac{2\pi i}{N_{\rm scan}}\right], A_{\rm delay}\,\mathrm{triangle}\left(\frac{i}{N_{\rm stroke}}\right)\right) \tag{32}$$

where r is the ring index and i is the sample inside the ring (such that the total sample number in the time-ordered data is $rN_{\rm scan} + i$), where $N_{\rm stroke} = 1\,920$, $N_{\rm spin} = P_{\rm spin}N_{\rm stroke} = 15\,360$ and $N_{\rm scan} = P_{\rm scan}N_{\rm spin} = 5\,898\,240$ are the number of samples per scan, spin and stroke respectively, and where $P_{\rm spin} = 8$ and $P_{\rm scan} = 384$ are the number of strokes per spin and spins per scan respectively.

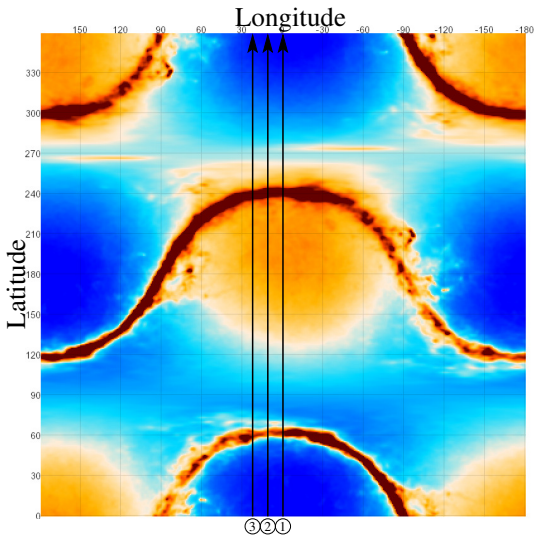

Figure 3: PIXIE's scanning pattern is particularly simple in ecliptic (extended) plate carrée (CAR) coordinates, where each scan moves at constant pixel velocity purely along the latidude axis. This allows an exact correspondence between samples and pixels. 3 example scans separated by 7.6 days are as black lines. The extended CAR coordinates here cover two mirror images of the full sky in order to show full scans without breaks.

Simple noise For simplicity, we will also assume that the detectors have independent white noise of equal amplitude. Neither of these are necessary, and can be easily relaxed in the future. Section 8.3 discusses the effect of correlated (1/f) noise on the PIXIE spectral maps.

With the nominal rates of 1024 detector samples per mirror stroke, the Fourier transform returns 512 synthesized frequency channels each 14.4 GHz wide, extending from DC to 7.4 THz. Scattering filters in the optical path limit the response at frequencies above 6 THz. Dispersion within the FTS from the finite spread of angles within the beam washes out the fringe amplitude at comparable frequencies. Synthesized channels at frequencies above ∼6 THz thus contain noise but no signal, providing a convenient check of the instrument noise.

6.2 Orthogonalization

It would have been very convenient if the stroke, spin and scan motions were orthogonal, so that the telescope didn't spin during a stroke and didn't scan during a spin. That would allow us to demodulate each of them independently. Rather than have stroke, spin and pointing change smoothly during each scan we would have $P_{\rm scan}$ pointings (corresponding to our output pixels), each with $P_{\rm spin}$ spin angles measured, and for each of those $N_{\rm delay}$ mirror positions.

Figure 4 illustrates the situation. In the 3-dimensional space of latitude, spin angle and mirror position (corresponding to the horizontal, vertical and color axis in the figure), the scanning pattern traces out a skewed grid (A) instead of the orthogonal grid that would be convenient (E). However, as long as our signal is well-sampled in all directions in the grid we can use the samples we have to interpolate to the orthogonal grid we wish we had.

We start by undoing the effect of the scan motion during each scan (and stroke) by splitting our samples into groups with the same spin angle and mirror position. Letting d_i be the i'th sample of the time-ordered data d for a single detector for a single ring, we split into groups such that sample (pixel) p in group $g \in \{0, N_{\rm spin}-1\}$ corresponds to $i = pN_{\rm spin} + g$, and let the notation $d_{ps} \equiv d_{i=pN_{\rm spin}+g}$. Because the shorter time-scale parameters are constant within each group, they see a signal that changes smoothly as the telescope scans over the beam-smoothed sky (i.e. as p changes while g is fixed), and this makes it easy to interpolate. Since the ring time-ordered data as a whole is periodic each of these evenly sampled ring subsets is also periodic, so we can interpolate via Fourier shifting: Given an array a containing N samples and a discrete Fourier transform F, an array a' equal to a shifted downwards by Δ samples is given by

$$a'_j = a_{j+\Delta} = \Psi(\Delta)_{jk} a_k \equiv F^{-1}_{jf} e^{-2\pi i f \Delta/N} F_{fk} a_k \tag{33}$$

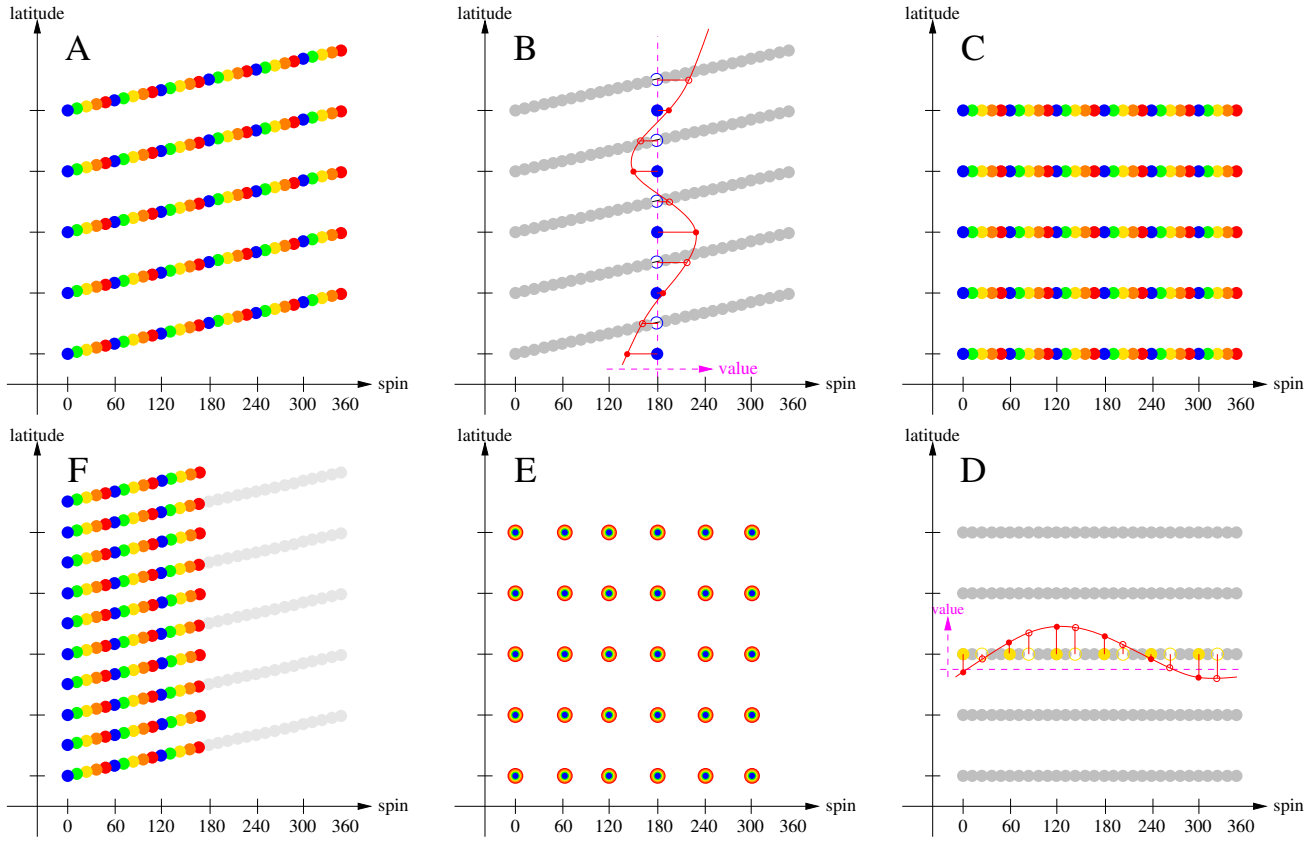

Figure 4: Orthogonalization of the scan, spin and stroke motions. PIXIE scans in circles on the sky, so the signal is periodic during a scan. It also spins and strokes. In isolation the signal would also be a periodic function of the spin angle and mirror stroke position, but because PIXIE scans while it spins, and spins while the mirror strokes these dimensions get mixed and the periodicity is lost on all but the scan timescale. **A**: Illustration of the mixing of the stroke (color), spin (x-axis) and scan (y-axis) dimensions in the PIXIE scanning pattern. **B**: A subset of points with the same stroke position and spin angle from periodic functions of the scan angle. The open circles represent the positions at which we have a measurement, while the filled ones are the positions we want to estimate. The red curve represents the smoothly varying signal inferred from the open points, which is used to interpolate the values at the filled points. The effect of this is to undo the scanning motion during each spin. Note that the red curve has its own x axis corresponding to the time-ordered data values. **C**: Spin and stroke are still mixed. **D**: We Fourier-interpolate between points with the same stroke position within a spin to undo the spin motion during each stroke. **E**: The scan, spin and stroke are now unmixed. The resulting timestream simulates what we would see if PIXIE stood still while the mirror strokes, then instantanously rotates to a new spin angle, strokes again, etc. and then instantanously moves to a new scan angle when the spin is done. **F**: The signal is spin-0 (I) or spin-2 (Q,U), so we can shorten the interpolation distance and decrease the pixel size by mapping the $180° - 360°$ interval to the $0° - 180°$ interval in spin angle.

which defines the Fourier-shift matrix $\Psi(\Delta)$. Using this, the scan drift corrected tod d' is given by:

$$\mathbf{s}^{\rm shift}_{rpg} = \Psi\big(g/N_{\rm spin}\big)_{pp'}\mathbf{s}^{\rm det}_{rp'g} \tag{34}$$

corresponding to panel C in the figure. This involves interpolating a distance of up to $\frac{1}{2}\cdot 360^\circ \cdot N_{\rm spin}/N_{\rm scan} = 0.46875^\circ$ on the sky, of about half a PIXIE FWHM. We can halve the interpolation distance by exploiting the spin-2 nature of our signal: only half a spin rotation is needed to return to the same configuration (panel F). This spin-2 scan drift correction is identical to the one above, but with half the normal value of $N_{\rm spin}$.

Undoing the effect of PIXIE's spin during the mirror motion follows the same logic on shorter time scales. We now group by mirror position (panel D) such that

$$\mathbf{s}^{\rm ort}_{rs\delta} = \Psi\big(\delta/N_{\rm stroke}\big)_{ss'}\mathbf{s}^{\rm shift}_{rs'\delta} \tag{35}$$

with $i = sN_{\rm stroke} + \delta$, s being the number of completed strokes and δ being the index in the mirror displacement pattern.

The orthogonalized equivalent to eq. 32 is

$$\mathbf{s}^{\rm ort}_{rps\delta} = GR_{\rm stok}\Big(\frac{4\pi s}{P_{\rm spin}}\Big)\mathbf{s}^{\rm sky}_{rp\delta} \qquad \text{with} \qquad \mathbf{s}^{\rm sky}_{rp\delta} = \mathbf{s}^{\rm sky}\Big([l_r, b_p], A_{\rm delay}{\rm triangle}\Big(\frac{\delta}{N_{\rm stroke}}\Big)\Big) \tag{36}$$

and where $l_r = l_0 + r\Delta l$ is the longitude of ring r, $b_p = b_0 + \frac{2\pi p}{P_{\rm scan}}$ is the latitude of pixel p along the ring.

6.3 Spin demodulation

Now that position, spin angle and mirror position are independent, we can handle each of them separately. We start by demodulating the spin. Suppressing the indices r, p and δ to avoid excessive verbosity, and expanding $\mathbf{s}^{\rm sky} = [I, Q, U]$, equation 36 evaluates to

$$s^{\rm ort}_{ds} = \Big[G_{dI}I + (G_{dQ} - iG_{dU})e^{4\pi is/P_{\rm spin}}(Q + iU)\Big] \tag{37}$$

This is just a weighted sum of 3 orthogonal Fourier modes, and can be straightforwardly inverted as

$$I = \langle G^{-1}_{dI}s^{\rm ort}_{ds}\rangle_{ds} \qquad Q = {\rm Re}\langle G^{-1}_{dQ}e^{-4\pi is/P_{\rm spin}}s^{\rm ort}_{ds}\rangle_{ds} \qquad U = {\rm Im}\langle G^{-1}_{dQ}e^{-4\pi is/P_{\rm spin}}s^{\rm ort}_{ds}\rangle_{ds} \tag{38}$$

which is simply the gain-correct 0th Fourier mode and real and imaginary part of the 2nd Fourier mode.

6.4 Frequency response correction

PIXIE's response drops off as we approach 6 GHz (see section 2.4). We correct for this by dividing each frequency bin by the instrument frequency response function $\rho(\nu)$ evaluated at the bin center.

6.5 Mapmaker pseudo-python

The full source code of the map-maker can be found in the programs `tod2ring.py` and `ring2map.py` in `https://github.com/amaurea/pixie`, but the overall logic is summarized in the pseudo-code below.

```
map  = zeros([nfreq,{I,Q,U},nlat,nlon])
hits = zeros([nlat,nlon])
for each scan:
    d = unapply_tod_filter(scan.tod)
    d = unapply_sample_window(d)
    # Unapply scan drift during spin
    if spin == 1:
        d = d.reshape(ndet,scanspins,spinstrokes*strokesamps)
        d = fourier_shift(d, range(d.shape[-1])/d.shape[-1], axis=1)
    else: # spin-2 - could be modified to double resolution
        d = d.reshape(ndet,scanspins*2,spinstrokes*strokesamps/2)
        dhalf = fourier_shift(d, range(d.shape[-1])/d.shape[-1], axis=1)
```

```
        d[:,0::2], d[:,1::2] = dhalf, dhalf
    # Unapply scan and spin drift during stroke
    d = d.reshape(ndet,scanspins*spinstrokes,strokesamps)
    d = fourier_shift(d, range(d.shape[-1])/d.shape[-1], axis=1)
    # Decompose spin modulation into I (spin-0 part) and Q,U (spin-2 part)
    d = d.reshape(ndet,scanspins,spinstrokes,strokesamps)
    d = fft(d, axis=2)
    # Transform from autocorrelation into spectrum
    d = [d[:,:,0],d[:,:,2].real*2,d[:,:,2].imag*2]
    d = fft(d, axis=3)*2/strokesamps/dfreq
    # Take into account the detector polarization orientation and frequency response
    d = unapply_detector_response(d)
    add_to_sky(map,  scan.lon, d)
    add_to_sky(hits, scan.lon, 1)
map /= hits
output(map)
```

7 Performance

The software was tested on the Scinet GPC cluster. On a typical node with an 8-core Intel Xeon 2.5 GHz processor the simulator has a run time of about $T_{\rm sim} = 81$ sec $\cdot N_{\rm scan} N_{\rm sub}/N_{\rm core}$, and the map-maker has $T_{\rm map} = 23$ sec$\cdot N_{\rm scan}/N_{\rm core}$. A 192-scan run with 9 subsamples per sample, like the ones used in this article therefore takes about 40 CPU-hours. The full PIXIE scanning pattern, with 1369.7 scans per year, would take 286 CPU-hours per simulated year.

The large speed difference between the simulator and map-maker is partially due to the overhead from high spatial and spectral resolution simulations, which are necessary for investigating sub-pixel and sub-sample biases. If one is not interested in these, then disabling pixel window integration results in a factor ~ 7 speedup. Further speedups would be possible in a simulator that operates at the same spatial and spectral resolution as the final maps, such as the spectral cube design needed for spatially and spectrally varying beams (see section 4.1).

Since each scan takes 384 minutes to collect but only 23 CPU-seconds to map with this mapmaker, a single core would easily keep up with the data down-link from the instrument.

8 Results

We generated a simple two-component CMB + dust sky model as described in section 4.3.1-4.3.2. A 58 GHz slice of this model can be seen in figure 5. We then simulated scanning across this model with the accelerated scanning pattern described in section 3, which would result in 384 scans per orbit. However, since the scans are great circles, only half an orbit is needed to cover the whole sky. Our simulations therefore consist of 192 scans, each consisting of 5898240 samples for each of 4 detectors at 256 Hz.

Figure 6 shows an example of what the time-ordered data looks like on various time scales, here for a noiseless single detector, in both single and double barrel mode. The stroke and spin modulation makes the TOD quite different from that of standard CMB experiments, which have a smoothly varying signal on short time scales.

Figure 7 shows the corresponding maps we get after running these simulated scans through the mapmaker, compared to the input model at 58 GHz evaluated at the center of each pixel. Even under these idealized conditions the residual is not zero, though it is small: 500 mJy/sr for dust and much less for the CMB in T, compared to the 100 MJy/sr CMB monopole; and 5 mJy/sr in P, compared to 200 Jy/sr for the signal. This represents a -83dB error in T and -46dB in P. Figure 8 shows the signal and bias spectra for a single input pixel, compared to the expected instrument noise. These deviations are due to subsample effects, and would also be expected when analyzing real data. See appendix A for details, but for now it suffices to note that these biases are many orders of magnitude smaller than the instrument noise floor.

With the mapmaker successfully recovering the input signal in this ideal case, we next study the effect of some common and less common instrument imperfections on PIXIE's performance.

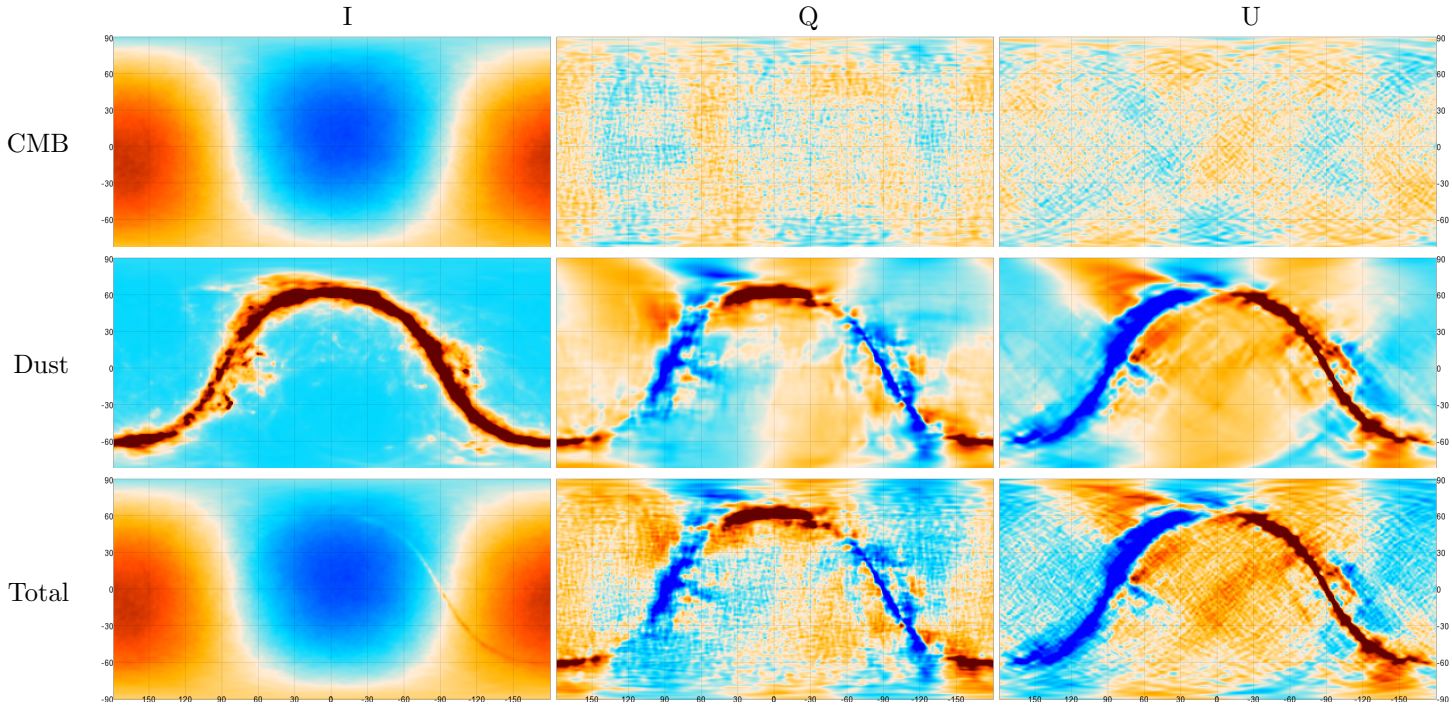

Figure 5: The input beam-smoothed sky model evaluated at 58 GHz in the CAR projection in ecliptic coordinates. The color range is ±400 kJy/sr in intentisty (I) and ±200 Jy/sr in polarization (P), except for dust I where it is ±5 kJy/sr. The monopole has been subtracted in each map for plotting purposes.

8.1 Intensity to polarization leakage

To first order, PIXIE is immune to intensity to polarization (I-to-P) leakage because any term sourced by I is not modulated as a spin-2 field as the telescope spins, and is therefore not classified as polarization. We confirm this in simulations, where even 100% I-to-P leakage in the optics have no effect on the result.

However, this spin-separation of polarization can itself become a source of polarization leakage. If the telescope barrel is not perfectly aligned with PIXIE's spin axis, then the beam will trace small circles in the sky during each spin. Any local intensity quadrupole around the point PIXIE is pointing at will show up as a spin-2 modulated signal in the time-ordered data, and will hence be interpreted as polarization. Alternatively, the same thing can happen if the barrel is correctly aligned, but the beam is elliptical.

We investigated ellipticity-induced leakage for a point source in figure 9 and for a cmb + dust map in figure 10, both for a highly elliptical beam with a flattening of 0.5. For each detector in isolation, the ellipticity results in a strong quadrupolar leakage pattern that completely dwarfs the intrinsic polarization. However, when combining detectors to make a full map this leakage is doubly canceled. Firstly, because the two detectors in a horn have the same I response but opposite polarization response, the leakage from each detector cancels. And secondly, the left and right horn also differ by an overall sign in their polarization sensitivity, leading to a second cancellation. All in all, I-to-P leakage is a third order effect in PIXIE, and is unlikely to be an important systemaic effect.

8.2 Beam circularization

PIXIE's spin around the boresight also circularizes the beam. In the ideal orthogonal case, where the telescope does not scan or stroke while spinning, every pixel would be observed equally at every spin angle, leading to perfect circularization. In practice, though, we need to rely on interpolation to simulate an orthogonal scanning pattern, and this relies on the signal changing smoothly as the spin angle changes in 22.5° steps (since there are 16 half-strokes per full spin)[13] [14]. But a very long and thin beam could in theory sweep over a small feature in

[13] This is for spin-2 orthogonalization. With spin-1, we get 8 full strokes per spin and hence 45° steps.

[14] While the autocorrelation function repeats every quarter-stroke, every other quarter-stroke is mirrored, so they do not form an equi-spaced dataset suitable for Fourier interpolation when orthogonalizing. Otherwise, we could have gotten both 32 orthogonalized spin angles would have been possible.

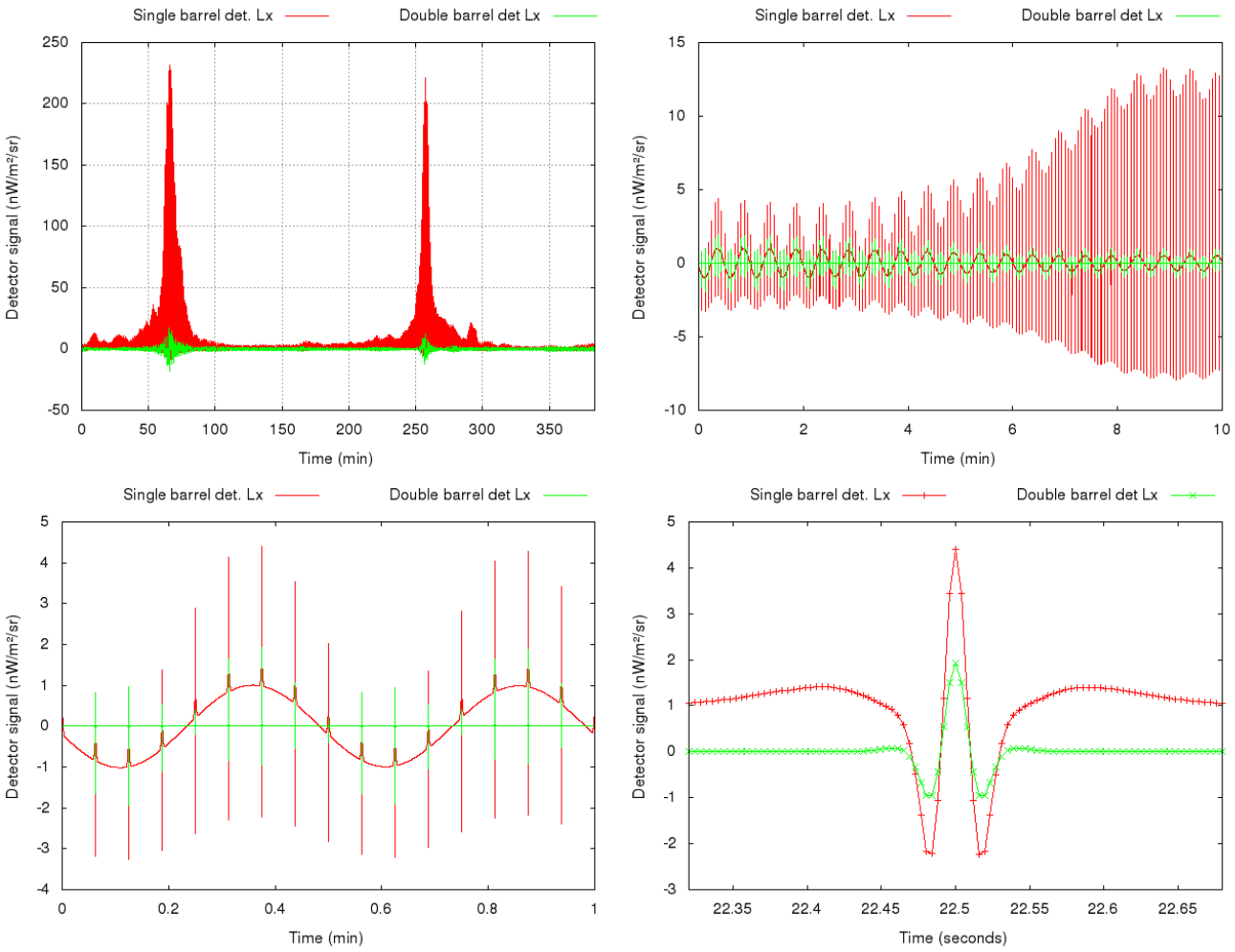

Figure 6: Noiseless simulated PIXIE time-ordered data for the Lx detector on various time scales in single (red) and double (green) barrel observing mode. *Top left*: A whole great-circle scan of the sky, starting at ecliptic coordinates $l = 0°$, $b = 0°$ and scanning in longitude. The two peaks are crossings of the galactic plane. *Top right*: Zoom on the first 10 minutes. We see that the signal is modulated on 3 time-scales: The sky signal changes on minute time-scales due to the scan; the polarization is modulated on 15 second time-scales due to PIXIE's spin; and the signal is modulated on second time-scales by the mirror stroke. *Bottom left*: Zoom on a single PIXIE spin. The slowly changing baseline is the DC signal, which PIXIE will not attempt to measure due to its susceptibility to 1/f noise. *Bottom right*: Zoom on a single mirror half-stroke, centered on $\Delta t = 0$. This is effectively a plot of the electric field's autocorrelation function at this position.

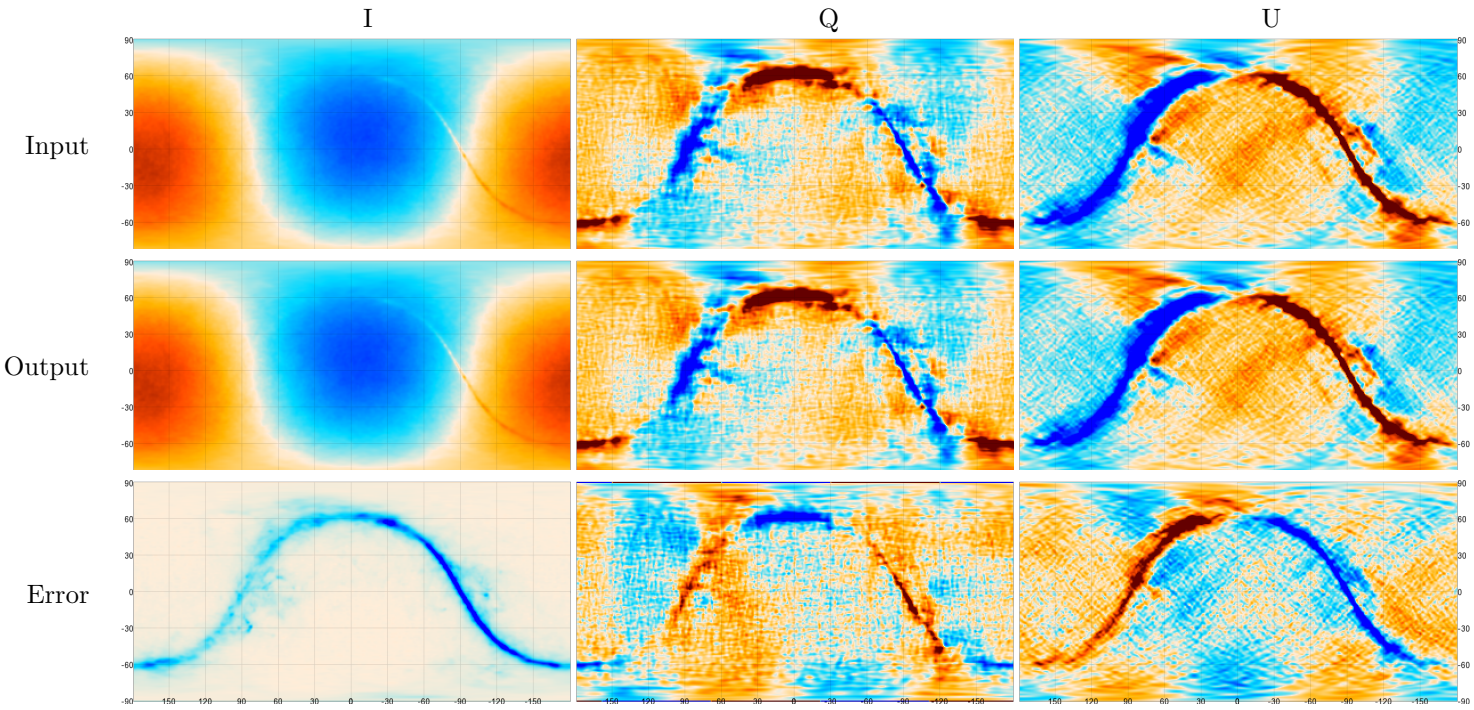

Figure 7: Simulator/map-maker spatial bias test. *Top row*: The beam-smoothed input map at 58 GHz. The color range is ±400 kJy/sr for I and ±200 Jy/sr for P. *Middle row*: The output map at 58 GHz. *Bottom row*: Difference between the mapmaking output maps and input maps at the same frequency for a noise-less simulation. The color range is ±500 mJy/sr for I and ±5 mJy/sr for P. These represent the bias of the simulator-map-maker combination. The biases are small compared to the instrument noise.

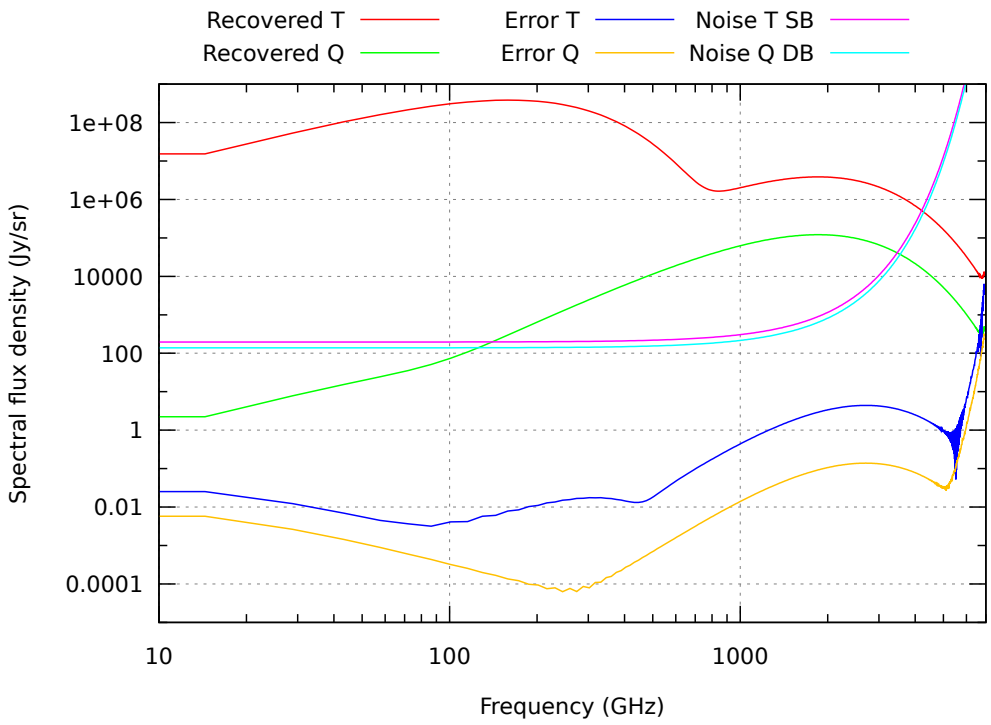

Figure 8: Simulator/map-maker spectral bias test. Recovered I and Q spectra and their errors for a noiseless simulation with 9 Gaussian quadrature subsamples per sample, compared to the PIXIE noise level. This is all for a single pixel at $l = 0°$,$b = 0°$. The U spectrum is similar to the Q one, but was left out to avoid clutter. The bias is ~ 100 times lower than the noise for $\nu < 500$ GHz and ~ 5 times lower than the noise at the worst point at 2 THz. At 200 GHz the bias is $\sim 10^{-10}$ of the signal in I and $\sim 10^{-6}$ of the signal in P. These errors are independent of observing mode.

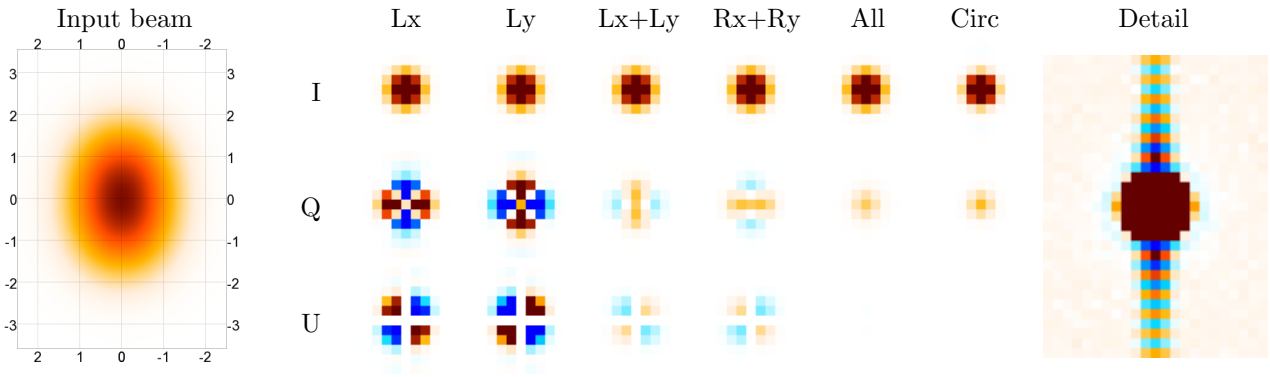

Figure 9: Simulation of a highly elliptical beam with a flattening of 0.5 observing a point source with 10% polarization in the Q direction. The beam is built up from 5 identical, circular, gaussian components with FWHM of 1.9 deg offset vertically with an interval of 0.475 deg. *Left*: Map of the instantaneous beam profile, with axis units of degrees. *Middle*: The PIXIE scanning pattern circularizes the beam efficiently, at the cost of a slight increase in beam size compared to the non-elliptical case. Beam ellipticity also introduces polarization leakage due to the spin-2 nature of an elliptical beam, but this is doubly suppressed in PIXIE. First, it's cancelled when combining detectors in each horn unless the two detectors have different beams, and secondly, it's cancelled when combining the signal from the two horns unless the two horns have different beams. In this simulation we used an unrealistically high 10% mismatch between x- and y-oriented detectors in each horn, making the first cancellation only 90% efficient. The Q and U color scale is 10% of the I color scale here. *Right*: Plotting the output beam in a restricted color range reveals a ringing pattern in the scan direction with amplitude $2.3{\cdot}10^{-3}r/1^\circ$ relative to the beam peak, where r is the distance from beam center. This also appears for a circular input beam, and is a manifestation of the subsample effects described in section A. The ringing makes it hard to quantify the amount of residual non-circularity, except by saying that it's $\lesssim 2.3 \cdot 10^{-3}$ of the circular component.

far shorter time than this. This would create complicated spatially dependent artifacts in the autocorrelation function.

Furthermore, even if the orthogonalization went perfectly, it would still only result in 16 discrete, evenly spaced spin angles[15] per pixel. The resulting beam is then the average over these 16 orientations, and so would not be perfectly radially symmetric, but would instead have an 16-fold angular symmetry.

These effects are illustrated in figure 11, for a multimodal beam with two circular components separated by 10°. The resulting beam is not circular, and has quite complicated sub-structure.

How important are these limitations in practice? As we can see in figure 9, even for a beam with an unrealistically large flattening of 0.5 any residual non-circularity is low enough that it is drowned out by sub-pixel effects.

8.3 Correlated noise

PIXIE's detector readout is expected to have a slowly varying 1/f noise component, with an $f_{\rm knee} \sim 1/\text{hour}$ or longer. 1/f noise usually manifests as correlated structures in the map, for example striping in the scanning direction. In PIXIE's case, though, we get a measurement of the spectrum every 7.5 seconds as the mirror strokes. As long as it is purely additive, slow drifts can be thought of as low-order polynomials vs mirror position for a single mirror stroke. As such, they are Fourier-transformed to low optical frequencies and affect only the DC component, or at worst the first few bins of the synthesized spectra, and do not propagate to spatial striping in the maps. We therefore expect PIXIE's maps/spectra to have only white noise.

To test this we simulated 1/f noise with power $(1 + [f/f_{\rm knee}]^\alpha)\sigma^2$, with $f_{\rm knee} = 0.1$Hz (hundreds of times higher than expected, but slower than the stroke frequency), $\alpha = -3$ and $\sigma = 83\sqrt{\text{s}}\text{fW/m}^2\text{/sr}$ per detector. As figure 12 shows, this results in noise that white both spatially and spectrally. This confirms our expectation that (additive) correlated noise should not be an issue for PIXIE.

[15] When using high-resolution mapping (see panel F in figure 4) this reduces to 8.

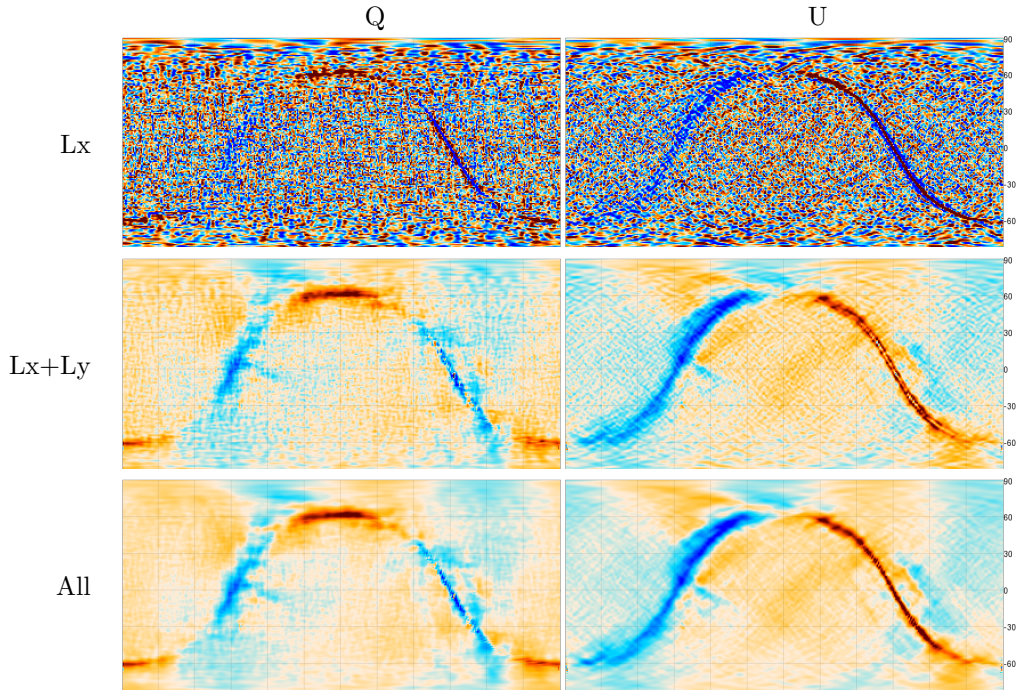

Figure 10: As figure 9, but for a cmb+dust simulation. *Top*: Q and U maps based on only the Lx detector. The maps are dominated by O(1) leakage of small-scale I. *Middle*: When coadding the Lx and Ly detectors the leakage is greatly reduced. If the two detectors have the same beam (as would be expected in the real instrument), then this cancellation would be perfect. In our simulation there is a 10% mismatch, so the leakage is only suppressed by 90%. *Bottom*: Map based on all four detectors (Lx+Ly+Rx+Ry). Because we assumed the same beams for the detectors in the left and right horns, the leakage cancels. Leakage would only survive if both the detectors in a horn are mismatched *and* the horns themselves are mismatched. The color scale is ±400 kJy/sr in I and ±500 Jy/sr in Q and U.

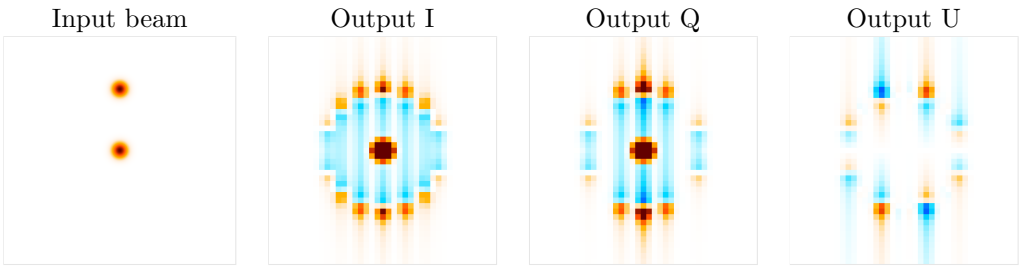

Figure 11: Beam circularization failure for a multimodal input beam. Each component has a FWHM of 1.9°, and they are separated by 10°. One would expect the off-center beam component to be smoothed into a smooth circle, but due to the limited amount of spin angles after orthogonalization the result is a dashed circle. Additionally, the sharp angular dependence of the beam results in interpolation failure during orthogonalization, which is responsible for the striping in the scanning direction. This failure mode is not relevant for realistic PIXIE beams.

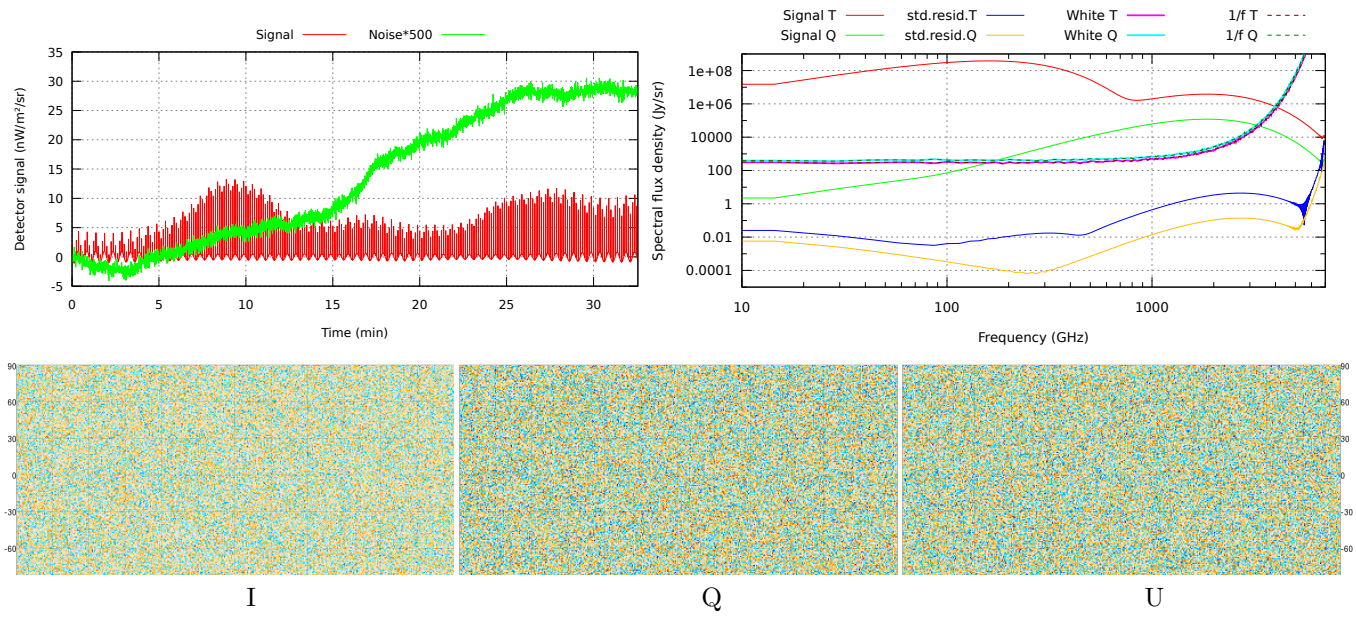

Figure 12: *Top left*: Example noise realization with 1/f-noise with $f_{\rm knee} = 0.1$ Hz, $\alpha = -3$ and $\sigma = 83\sqrt{\rm s}$ fW/m^2/sr per detector. This $f_{\rm knee}$ is several orders of magntiude larger PIXIE's expected value, resulting in strongly non-white noise on > 10 s time scales. *Top right*: The resulting noise RMS is 92Jy/sr per 15 GHz bin per $1^{\circ 2}$ pixel in I and 128Jy/sr in Q and U. These numbers take into account that our actual bins are slightly smaller than 15 GHz, and that our pixels are slightly smaller than $1^{\circ 2}$. Despite the high $f_{\rm knee}$, the resulting spectrum noise is indistinguishable from white. The spectrum (and map) has been rescaled to correspond to 15 months of data. *Bottom*: Map noise resulting from single barrel mapmaking with this noise sim. The color scale is ± 500 Jy/sr. Like in the spectrum, the map noise is practically white.

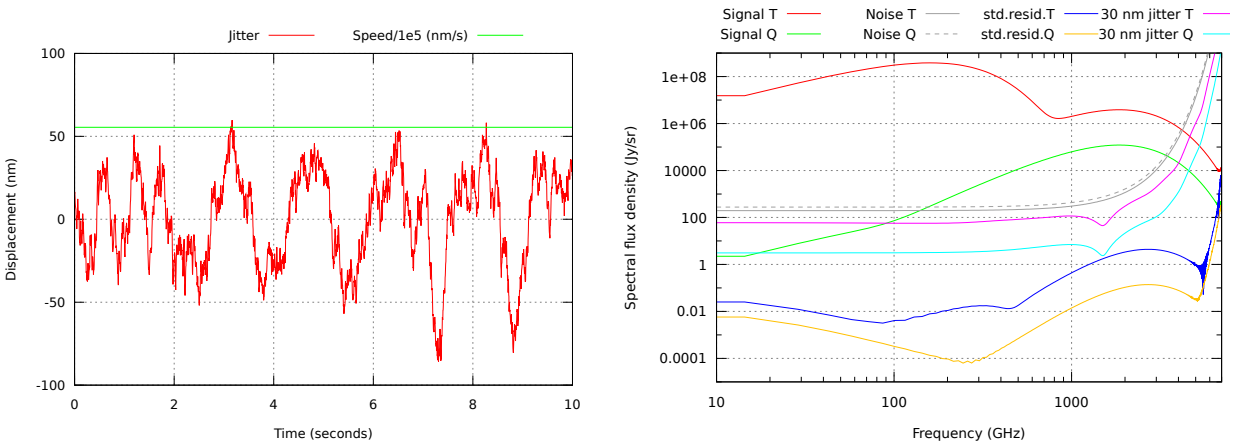

Figure 13: The effect of jitter in the mirror position. *Left*: We added noise consisting of a sum of 100 sine waves with random periods logarithmically distributed in the range 0.25 Hz to 1000 Hz with power proportional to f^{-1} and a combined RMS of $30\text{nm}\sqrt{\text{s}}$. This is a rough approximation of noise that is damped on long timescales by the mirror control system and on short timescales by the inertia of the mirror. An example of such a noise realization is shown in red, and compared to the mirror average displacement per second divided by 10^5. *Right*: The average single-pixel spectrum error caused by this jitter compared to the signal, PIXIE noise and subpixel/subsample bias. A mirror jitter of the form and magnitude simulated here would be the largest of the systematic effects investigated in this paper. This plot is for single barrel mode, but the jitter noise curve in polarization is the same in double barrel mode.

8.4 Sub-pixel effects

Anisotropy on scales smaller than PIXIE's beam, including CMB anisotropy as well as point sources, will affect the map making. Scanning the beams across the sky causes point sources to enter or exit the beam during the course of a single mirror stroke, creating signal variations on time scales short compared to the mirror stroke. Signals on short time scales (high spatial frequencies) are Fourier-transformed to high frequencies in the synthesized spectra and primarily affect channels above 6 THz containing little true sky signal. See appendix A a fuller discussion.

8.5 Mirror jitter

In PIXIE's map-making we model the interferometer path delay as changing at a constant rate in a triangle wave pattern. But in a real experiment the mirror is a physical device that cannot turn around instantly, and which will end up vibrating and jittering at some level. The exact performance that can be expected from the mirror is still uncertain, but according to Nagler et al. (2015), a jitter in the path difference of $\sim 30\text{nm}\sqrt{\text{s}}$ has been achieved.

We simulated jitter at this level by adding noise consisting of a sum of 100 sine waves with random periods logarithmically distributed in the range 0.25 Hz to 1000 Hz with power proportional to f^{-1} and a combined RMS of $30\text{nm}\sqrt{\text{s}}$ to the path delay in the simulator. This is a rough approximation of noise that is damped on long timescales by the mirror control system and on short timescales by the inertia of the mirror. The resulting spectra are shown in figure 13. Jitter both smoothes the autocorrelation function and acts as an extra noise component, but as the figure shows the latter dominates for PIXIE.

The jitter shows up as an extra white noise component in the spectra, and unlike the other effects we have investigated, this contribution to the noise is not negligible. In total intensity it is about half as as high as the expected instrument noise, while it's about two orders of magnitude below the noise in polarization. The jitter level at which the jitter noise and instrument noise are equal are $0.10\mu\text{m}\sqrt{\text{s}}$ for I, $2.2\mu\text{m}\sqrt{\text{s}}$ for P (single barrel) and $3.1\mu\text{m}\sqrt{\text{s}}$ for P (double barrel).

One might hope that double barrel mode would be less affected by jitter noise, as it cancels the huge total intensity signal, and hence could prevent it from contributing to this noise term. However, the opposite polarization sign for the two detectors in each horn cancels the total intensity contribution to the polarization jitter

noise even in single barrel mode. Mirror jitter is therefore approximately as important in double barrel mode[16]. Ensuring a low mirror jitter should be a high priority in the PIXIE hardware design.

9 Conclusion

We have developed time-ordered data simulator and map-maker for the proposed PIXIE experiment, and used them to test the impact of subpixel bias, intensity to polarization leakage, beam ellipticity/off-axis pointing, correlated noise and mirror jitter. We find PIXIE to be remarkably robust against all these effects, with the exception of mirror jitter, which is a potential concern. At jitter levels above $0.10\mu\mathrm{m}\sqrt{\mathrm{s}}$ for I or $3.1\mu\mathrm{m}\sqrt{\mathrm{s}}$ for P, the jitter rather than detector performance becomes the limiting factor for the instrument's sensitivity.

This simulation framework was developed for PIXIE, but can be adapted for any similar CMB satellite mission operating with a Fourier transform spectrometer.

Acknowledgements

We would like to thank T. Louis for helpful comments during the writing of the article. The Flatiron Institute is supported by the Simons Foundation.

References

Abitbol, M. H., Chluba, J., Hill, J. C., & Johnson, B. R. 2017, arXiv:1705.01534, MNRAS, 471, 1126, Prospects for measuring cosmic microwave background spectral distortions in the presence of foregrounds

ACT Collaboration. 2017, arXiv:1610.02360, J. Cosmology Astropart. Phys., 6, 031, The Atacama Cosmology Telescope: two-season ACTPol spectra and parameters

Bennett, C. L., et al. 2013, arXiv:1212.5225, ApJS, 208, 20, Nine-year Wilkinson Microwave Anisotropy Probe (WMAP) Observations: Final Maps and Results

BICEP2/Keck and Planck Collaboration. 2015, arXiv:1502.00612, Physical Review Letters, 114, 101301, Joint Analysis of BICEP2/Keck Array and Planck Data

Calabrese, E., Alonso, D., & Dunkley, J. 2017, arXiv:1611.10269, Phys. Rev. D, 95, 063504, Complementing the ground-based CMB-S4 experiment on large scales with the PIXIE satellite

Fixsen, D. J., Cheng, E. S., Gales, J. M., Mather, J. C., Shafer, R. A., & Wright, E. L. 1996, astro-ph/9605054, ApJ, 473, 576, The Cosmic Microwave Background Spectrum from the Full COBE FIRAS Data Set

Henning, J. W., et al. 2017, arXiv:1707.09353, ArXiv e-prints, Measurements of the Temperature and E-Mode Polarization of the CMB from 500 Square Degrees of SPTpol Data

Kogut, A., Fixsen, D. J., & Hill, R. S. 2015, arXiv:1503.04206, Journal of the Optical Society of America A, 32, 1040, Polarization properties of a broadband multi-moded concentrator

Kogut, A., et al. 2011, arXiv:1105.2044, J. Cosmology Astropart. Phys., 7, 025, The Primordial Inflation Explorer (PIXIE): a nulling polarimeter for cosmic microwave background observations

Kogut, A. J. & Fixsen, D. J. 2018, arXiv:1801.08971, Journal of Astronomical Telescopes, Instruments, and Systems, 4, 014006, Polarized beam patterns from a multimoded feed for observations of the cosmic microwave background

Nagler, P. C., Fixsen, D. J., Kogut, A., & Tucker, G. S. 2015, arXiv:1510.08089, ApJS, 221, 21, Systematic Effects in Polarizing Fourier Transform Spectrometers for Cosmic Microwave Background Observations

Planck Collaboration. 2013, arXiv:1303.5062, Planck 2013 results. I. Overview of products and scientific results

[16]Double barrel mode is more robust to I-to-P leakage, so in the presence of uncancelled I-to-P leakage, the single barrel polarization jitter noise would increase above the level indicated in figure 13, while the double barrel jitter noise would stay as it is. So in that case double barrel mode would be an improvement.

Reinecke, M. & Seljebotn, D. S. 2013, arXiv:1303.4945, A&A, 554, A112, Libsharp - spherical harmonic transforms revisited

Smoot, G. F., et al. 1992, ApJ, 396, L1, Structure in the COBE differential microwave radiometer first-year maps

Thorne, B., Dunkley, J., Alonso, D., & Næss, S. 2017, arXiv:1608.02841, MNRAS, 469, 2821, The Python Sky Model: software for simulating the Galactic microwave sky

A Sub-pixel effects

As we saw in section 8, even ideal, noiseless simulations result in low-level deviation from the input, as seen in map-space in figure 7 and in the spectrum in figure 8.

We believe that these biases are almost entirely due to sub-pixel effects. During the orthoganalization procedure (section 6.2) interpolation is needed to go from the observed samples to the idealized, orthogonal samples. The map-maker uses Fourier-interpolation to do this, but the simulator uses bicubic spline interpolation to generate samples that fall between input pixels. Hence, the simulator and map-maker are making different assumptions about how the signal behaves on sub-pixel scales, and this mismatch leads to map $\rightarrow$ tod and tod $\rightarrow$ map not being exact inverses of each other. Figure 14 demonstrates this effect for a simpler 1-dimensional case.

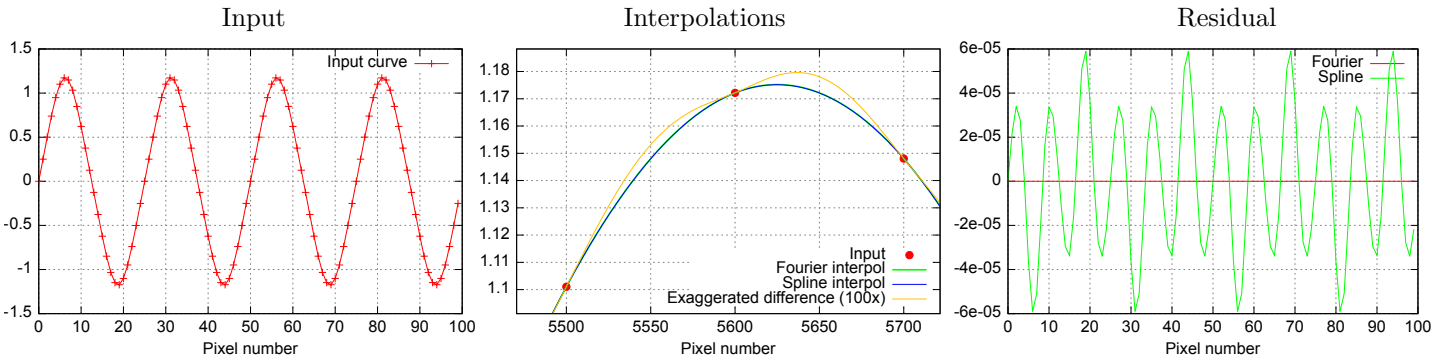

Figure 14: 1-dimensional toy example of sub-pixel mismatch bias. *Left*: The input data set, which is a densely sampled sine wave with 25 points per wavelength. *Middle*: Two models for the sub-pixel behavior of the data set (Fourier and spline interpolation) disagree slightly. *Right*: The residual after shifting the dataset right by half a sample (i.e. half-way between the red points in the middle panel) using Fourier (red) and spline (green) interpolation, and then back again using Fourier interpolation in both cases. When the forwards and backwards methods do not match, the result is biased.

Sub-pixel errors also occur during the sample window deconvolution. The sample window is simulated by integrating sub-samples using gaussian quadrature, which amounts to assuming that the sub-sample behavior is described by a low-order polynomial. However, the deconvolution is done by dividing by a sample window in Fourier space, which assumes that the sub-pixel behavior is given by sines and cosines bandlimited by the sampling frequency.

We investigate the effect of these sub-pixel effects in figure 15, where we first remove the sample window (both in simulation and map-making), and then make the map spatially homogeneous to eliminate sub-pixel effects. After removing both of these, we are left with a relative error of $\sim 10^{-15}$, which we attribute to floating point errors.

These sub-pixel effects would not have appeared if the simulator and map-maker both made the same assumptions about sub-pixel behavior, which would have been the case for a simpler simulator. That would, however, have been misleading. The real sky is neither Fourier-interpolated nor bicubic-interpolated, and so this kind of sub-pixel mismatch is unavoidable when analyzing actual data. The mismatch between Fourier-interpolation and bicubic interpolation is not exactly the same as what one can expect for the real data, but it is a good approximation for it.

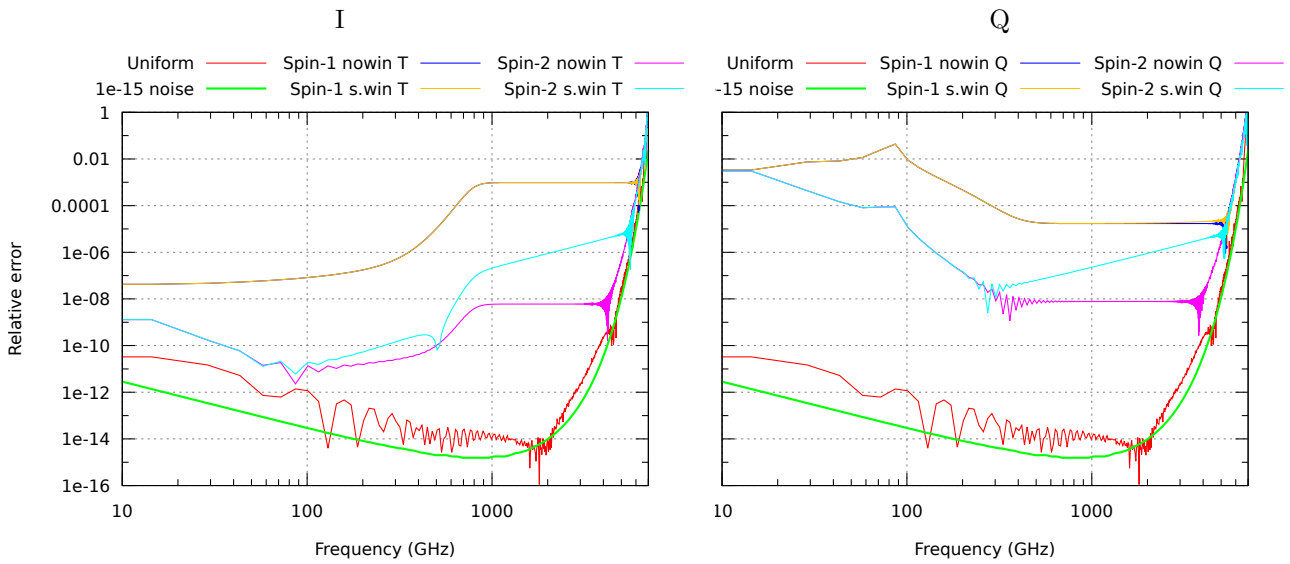

Figure 15: The effect of sample window and Fourier shift distance on the mapmaking bias. Both of these are examples of sub-pixel bias. The sample window error comes from the mismatch between the gaussian quadrature that is used to integrate the sample window and the Fourier-space deconvolution that is used to remove it. It rises with frequency and is a $\sim 10^{-7}$ error at 1 THz. The Fourier shift error comes from the mismatch between the high-res bicubic sub-pixel behavior of the sky in the simulator and the bandlimited Fourier model used in the map-maker. It has a surprisingly large dependence on the interpolation distance. Spin-1 Fourier shifting has twice the interpolation distance of Spin-2 Fourier shifting, but $10^3 - 10^4$ times as large a bias. The red curve shows the error for a monopole-only sky when using no sample window, demonstrating that aside from sub-pixel biases the accuracy is close to double precision float error. The relative Q error is high at low frequency because the signal itself becomes very small there. The feature at 90 GHz is due to Q changing sign there for this pixel.